Master's thesis
Master's Programme in Theoretical and Computational Methods

Simulating Bubble Nucleation in the Electroweak Phase Transition

Anna Kormu

August 7, 2020

Supervisors: Oliver Gould, David Weir,

Examiners: Oliver Gould, David Weir,

UNIVERSITY OF HELSINKI
FACULTY OF SCIENCE

HELSINGIN YLIOPISTO
HELSINGFORS UNIVERSITET
UNIVERSITY OF HELSINKI
MATEMAATTIS-LUONNONTIETEELLINEN TIEDEKUNTA
MATEMATISK-NATURVETENSKAPLIGA FAKULTETEN
FACULTY OF SCIENCE

Tiedekunta – Fakultet – Faculty	Koulutusohjelma – Utbildningsprogram – Degree programme
Faculty of Science	Master's programme in Theoretical and Computational Methods

Tekijä – Författare – Author

Anna Kormu

Työn nimi – Arbetets titel – Title

Simulating Bubble Nucleation in the Electroweak Phase Transition

Työn laji – Arbetets art – Level	Aika – Datum – Month and year	Sivumäärä – Sidoantal – Number of pages
Master's thesis	August 2020	86

Tiivistelmä – Referat – Abstract

First order electroweak phase transitions (EWPTs) are an attractive area of research. This is mainly due to two reasons. First, they contain aspects that could help to explain the observed baryon asymmetry. Secondly, strong first order PTs could produce gravitational waves (GWs) that could be detectable by the Laser Interferometer Space Antenna (LISA), a future space-based GW detector. However, the electroweak PT in the Standard Model (SM) is not a first order transition but a crossover. In so-called beyond the SM theories the first order transitions are possible. To investigate the possibility of an EWPT and the detection by LISA, we must be able to parametrise the nature of the PT accurately.

We are interested in the calculation of the bubble nucleation rate because it can be used to estimate the properties of the possible GW signal, such as the duration of the PT. The nucleation rate essentially quantifies how likely it is for a point in space to tunnel from one phase to the other. The calculation can be done either using perturbation theory or simulations. Perturbative approaches however suffer from the so-called infrared problem and are not free of theoretical uncertainty. We need to perform a nonperturbative calculation so that we can determine the nucleation rate accurately and test the results of perturbation theory.

In this thesis, we will explain the steps that go into a nonperturbative calculation of the bubble nucleation rate. We perform the calculation on the cubic anisotropy model, a theory with two scalar fields. This toy model is one of the simplest in which a radiatively induced transition occurs. We present preliminary results on the nucleation rate and compare it with the thin-wall approximation.

Avainsanat – Nyckelord – Keywords

Phase transition, gravitational waves, bubble nucleation, lattice simulations, early universe

Säilytyspaikka – Förvaringställe – Where deposited

Kumpula campus library

Muita tietoja – Övriga uppgifter – Additional information

Contents

Chapter 1

Introduction

The Standard Model (SM) of particle physics provides a comprehensive model of the universe. It has been proven to be accurate in its predictions and the last missing piece, the Higgs boson, was found by the Large Hadron Collider (LHC) in 2012 [1, 2]. The LHC is a particle collider located at the border of France and Switzerland and is a part of Europe's biggest particle physics collaboration, CERN. However, we also know that the SM falls short in certain aspects and is not the complete story. It fails to provide an answer to questions such as the origin of baryon asymmetry and the existence of dark matter, to name but two. Physicists are therefore on the hunt for theories beyond the Standard Model (BSM). One place to look for interesting new physics are gravitational waves (GWs) from phase transitions (PTs) in the early universe. They are a new way of looking at BSM theories, with particle colliders, such as the LHC, one can theoretically always reach higher and higher energies but in practise this becomes impossible. Thus, GW detectors are promising as a completely new approach.

Gravitational waves have been detected from black holes and from neutron star mergers by LIGO and Virgo [3–5]. Both LIGO and Virgo are interferometric detectors, based in the US and Italy respectively. However, both detectors face limitations due to their earthly location. To name a few, eliminating noise sources can be difficult and the arm length of the detector itself is rather limited. To eliminate both of these problems and thus detect GWs from lower frequencies we need to go somewhere quieter, to space. The first space-based gravitational wave detector LISA (Laser Interferometer Space Antenna) is supposed to launch in the early 2030's [6]. With LISA we might be able to detect strong

first order PTs, since their stochastic GW signature would lie in the frequency range of LISA [7], see Fig. 1.1. The stochastic GW signature is different from the signal that LIGO is able to detect, it is a continuous signal that consists of relic GWs from the very early universe.

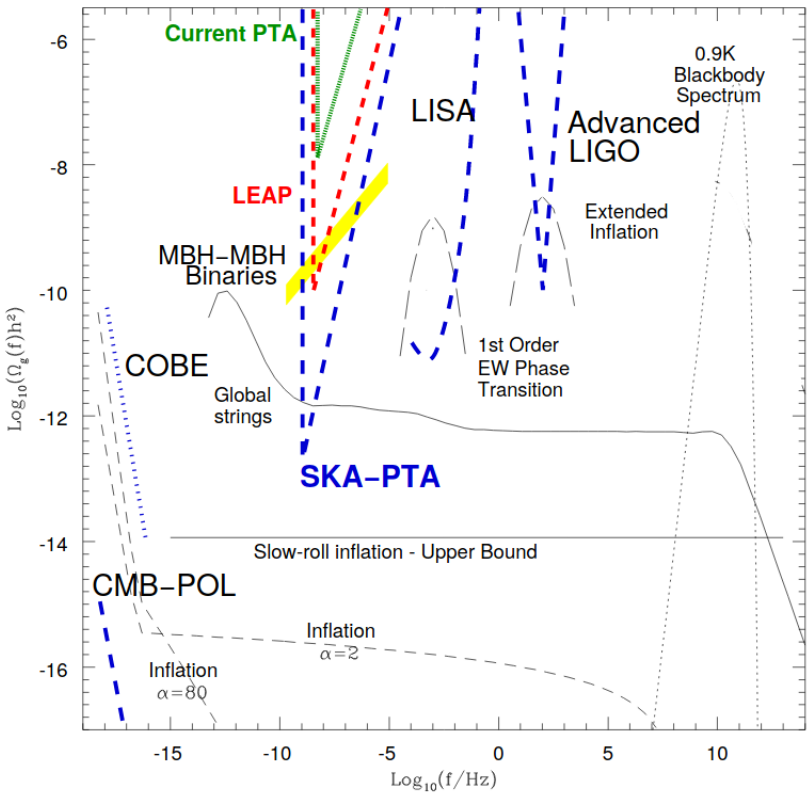

Figure 1.1: The possible stochastic GW background sources that could be detectable by current and near-future detectors. From left to right, the pulsar timing arrays (PTA), LISA and LIGO. Note that this graph is not up-to-date anymore, but we present it here for the sake of illustration of the different frequency ranges. Image credit Ref. [8].

So what are these cosmological PTs? As the universe cools down it may undergo a phase transition. Think of water freezing, another first order PT, but rather familiar to us from everyday life. Our phase transition would of course be one of a cosmological variety and would have happened in the very early universe, roughly one nanosecond after the Big Bang. As the universe gets colder from the initial hot plasma state, the electroweak sym-

metry $SU(2)_L \times U(1)_Y$ is spontaneously broken to $U(1)_{em}$. We know that at high enough energy scales at least the electromagnetic and weak interaction are unified. In order for them to become distinct at lower energies, we need symmetry breaking to occur [9, 10]. It is also speculated that at higher energy scales a further unification of the electroweak and strong force is observed, called Grand Unification.

This thesis is structured as follows: first we will take a short dive into the dynamics of the phase transition and briefly talk about baryogenesis. We will go into greater detail about the production of gravitational waves. The main focus of this thesis will be the calculation of the bubble nucleation rate using lattice simulations. In Chapter 2 we will briefly go though the analytical method of obtaining the bounce solution and the nucleation rate at zero and at finite temperature. The bubble nucleation rate is tied to the gravitational wave production rate. Chapter 3 focuses solely on GWs and the different sources an EWPT could produce. Next, in Chapter 4, we will briefly introduce the simulation methods and tools we have used. Chapter 5 describes the lattice calculation in detail, starting from the Monte Carlo evaluation and ending with the real time evolution. Chapter 6 then provides us with a further explanation of the model we have looked at, the cubic anisotropy model, and the simulation results. Finally, in Chapter 7, we will discuss the difference between the perturbative analysis and simulation results. Furthermore, we will discuss the future of these calculations.

1.1 The electroweak phase transition

The electroweak PT starts when the universe is hot and in the radiation dominated era, around 10^{-9} seconds after the Big Bang. As the universe then gets colder the thermal plasma goes through a phase transition. In the symmetric state we have the electroweak gauge symmetry and in the broken phase only the electromagnetic remains. We are interested in these phase transitions because of the information they could provide on physics at energy scales that are not reachable by current particle collider experiments [11]. However, one should note that particle colliders and GW detectors are complementary rather than competitive. The detection of a GW signal from a first order PT would also shed

light on the nature of the PT. The dynamics of the transition depend on the effective potential at a finite temperature [12].

In the Standard Model, the electroweak phase transition is a crossover [13–15] that happens at the critical temperature of 160 GeV [16]. Crossover means that there are no points where the two distinct phases coexist and thus there is no possibility for gravitational wave production from EWPT in the SM. For other possible physical phenomena, such as cosmic strings, this is not necessarily true. For the transition to be of first order in the SM the Higgs mass should be less than 80 GeV, which of course is well below the observed mass of 125 GeV [2]. Hence, no first order transitions can occur in the SM at the electroweak scale.

However, if we go to beyond the SM theories, the transition could very well be of first order and thus remains as an attractive theory. There are two main reasons for this. First, it could help to solve the observed baryon asymmetry that the SM alone does not explain [17]. The second reason we have already mentioned, this particular transition is in the correct detection range for LISA. The PT has to be of first order, since neither second order transitions nor a crossover does produce GWs via this mechanism. Even if this turns out to be the nature of the transition and LISA does not detect a signal, this could be used to constrain BSM theories [11].

We will now discuss the shape of the effective potential $V_{\text{eff}}(\phi, T)$ that determines the nature of the transition. The effective potential is simply the energy density of a homogeneous state at some temperature T. The behaviour of the potential depends on the order of the PT and is characterised by the so called order parameter. An order parameter is some parameter that has a discontinuity when the phase transition happens. The critical temperature T_c then tells us when two phases have the same free energy. In the crossover scenario the meaning of the critical temperature is slightly different, it is the temperature where the rate of change of the phase is the fastest.

Initially, the universe is very hot and the minimum of the potential V_{eff} sits at $\phi = 0$, see Fig. 1.2. In the first order transition the case is the following, see Fig. 1.2a. As the universe cools down and reaches the critical temperature $T = T_c$, the potential develops a barrier and the minimum becomes degenerate. When $T < T_c$ the minimum at $\phi = 0$

becomes metastable and the Universe is trapped in a false vacuum (symmetric phase). In order to get to the real minimum of the effective potential (broken phase), the transition to the true vacuum has to overcome the barrier in the potential. This can be achieved via either thermal fluctuations or quantum tunneling. Bubbles of the true vacuum then nucleate.

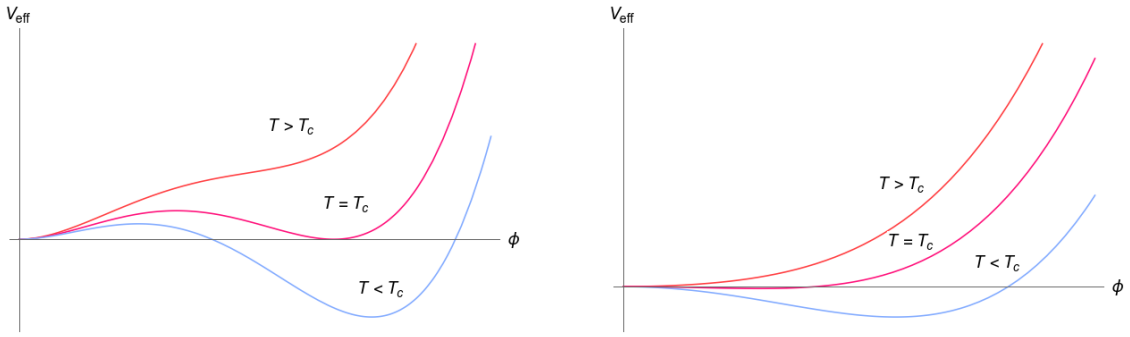

(a) First order PT

(b) Second order PT or a crossover

Figure 1.2: The effective potential $V_{\text{eff}}(\phi, T)$, where T_c is the critical temperature. On the left we have the first order PT with a clear barrier in the potential. On the right the smooth second order transition.

When some regions in space have tunneled through the barrier and ended up in the true vacuum state (broken phase) the bubbles start to expand, see Fig. 1.3. The bubbles expand due to a pressure difference on the walls and collide with each other until they have converted the whole space to the true vacuum state[1]. The pressure difference between the bubble walls is due to the surrounding plasma. Because the bubbles are spherically symmetric they cannot produce GWs. The collisions between the bubbles however break this symmetry and thus produce GWs [18]. In Fig. 1.2b we have the shape of the effective potential when the transition is of second order or a smooth crossover. The potential does not have a barrier and thus no bubbles are nucleated.

To describe the nature of the acquired GW spectrum from a first order PT only a few parameters are needed: the bubble wall velocity, strength of the transition, the temperature when the bubbles are nucleated and inverse duration of the PT. The energy available to source these GWs depends on the model but can be more generally thought of as the

[1]If they expand faster than the expanding universe.

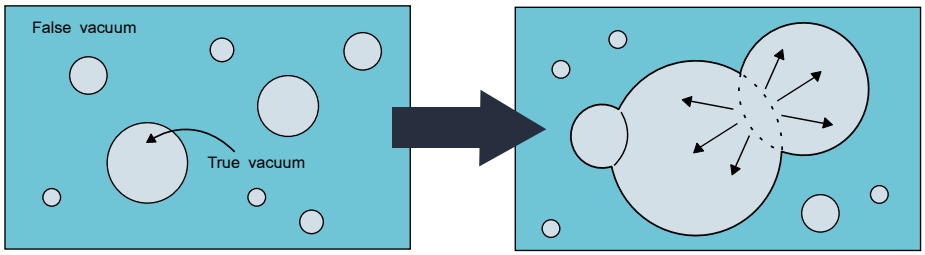

Figure 1.3: True vacuum bubbles nucleating and colliding with each other. The bubbles of the true vacuum expand and convert all of space to the broken phase.

latent heat. However, as we will soon see, the calculation and physics behind the GW spectrum are non-trivial. While we can use perturbation theory, simulations are a more reliable way of estimating the parameters. It is known that at high temperatures perturbation theory faces the so called infrared problem [19], which will be discussed later. With lattice field theory it is possible to avoid this and get more precise and reliable results, even at high temperatures.

1.2 Baryogenesis

Why is there more matter than antimatter in the observable universe? Baryogenesis is one of the ways that this asymmetry could have formed. As of now, we do not know how this process could have happened. However, the EWPT could provide us with some answers [17, 20]. Here we will shortly summarise the main aspects of baryogenesis and specifically focus on the possibility that baryogenesis occurred in connection with the EWPT. One should note that there are other mechanisms for generating the baryon asymmetry, such as the leptongenesis, see Ref. [21]. However, none of them can be tested by current or near future particle colliders. This makes electroweak baryogenesis (EWBG) attractive to look at, since experimental verification still remains a possibility, for example by measuring the anomalous dipole moment [22].

The asymmetry is usually described by a quantum number called the baryon number, for

a review see Refs. [23, 24]. It can be written as the baryon-to-photon ratio

$$\eta \equiv \frac{n_B - n_{\bar{B}}}{n_\gamma}, \tag{1.1}$$

where n_B and $n_{\bar{B}}$ denote the number density of baryons and antibaryons and n_γ is naturally the number of photons.

Alternatively it can be written using the entropy density s as [25]

$$B \equiv \frac{n_B - n_{\bar{B}}}{s} = (8.6 \pm 0.09) \times 10^{-11}, \tag{1.2}$$

where $s \approx 7.04 n_\gamma$. When referring to the baryon number, we will use the latter definition of B.

Baryon asymmetry means that at some point during the early universe not all baryons and antibaryons annihilated with each other and this created the discrepancy. Thus, as one might have observed, matter still exists in this universe due to this. In order for the generation of baryon asymmetry to be possible three conditions have to be satisfied. These are called the Sakharov conditions, proposed by Andrei Sakharov in 1967 and they are [26]:

1. Violation of the baryon number conservation
2. Violation of C and CP symmetries
3. Deviation from thermal equilibrium

The first condition is reasonably self explanatory, the universe starts from a baryon symmetric universe where the baryon number is zero. Later, this is violated and we end up having a non-zero baryon number, representing the baryon asymmetric universe.

Secondly, if we claim CPT invariance the net baryon number would remain as zero, hence breaking of at least charge conjugation (C) and charge-conjugation parity (CP)

symmetries must occur. Breaking the parity symmetry (P) is optional. We will now denote[2] the scattering amplitude for each process i as Γ_i and we also know that $B_i(p) = -B_i(\bar{p})$. Now, let us briefly look at the following equation

$$\Delta B = (B_3 + B_4 - B_1 - B_2)(\Gamma_1 - \Gamma_2 - \Gamma_3 + \Gamma_4). \tag{1.3}$$

If we apply the rules found in Fig. 1.4 we see that the change in the baryon number will be $\Delta B = 0$ if we do not break the C and CP symmetries.

Finally, the third condition must hold because in thermal equilibrium there is no generation of net baryon number. This is relatively straightforward to prove, we will denote $B = \langle \hat{B} \rangle$ as the expectation value of the baryon operator. The density operator in thermal equilibrium can be written as $\rho = \exp\left(-\hat{H}/T\right)$, where $\hat{H}$ is the Hamiltonian and θ is a CPT-transformation so that $\theta \hat{H} \theta^{-1} = \hat{H}$ and $\theta \hat{B} \theta^{-1} = -\hat{B}$. Now writing the expectation value in the trace formalism we get [27]

$$\begin{aligned} \langle \hat{B} \rangle &= \text{Tr } e^{-\hat{H}/T} \hat{B} \\ &= \text{Tr } e^{-\hat{H}/T} \theta^{-1} \theta \hat{B} \theta^{-1} \theta \\ &= \text{Tr } \theta e^{-\hat{H}/T} \theta^{-1} \theta \hat{B} \theta^{-1} \\ &= -\langle \hat{B} \rangle. \end{aligned} \tag{1.4}$$

This simply cannot be, thus $\langle \hat{B} \rangle = 0$ and we must differ from the thermal equilibrium. The EWPT provides a departure from thermal equilibrium if it is a strong first order transition.

Now that we have briefly reviewed the conditions that need to be met in order to produce a baryon asymmetry we will discuss the specifics of the EWBG dynamics. First, we however need to understand what sphalerons are. A sphaleron is a "ready to fall" solution to the field equations. Compared to instantons, solutions that tunnel, the sphalerons can be thought as going up and down the barrier classically, see Fig.1.5 [28].

[2]Note that later we will use Γ for the nucleation rate!

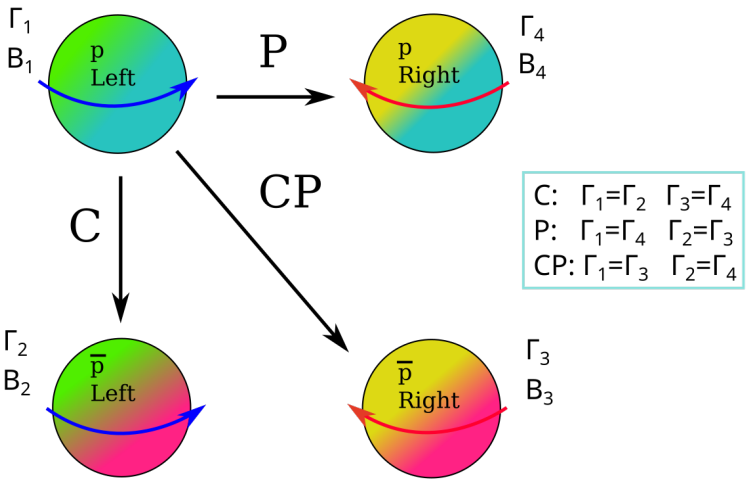

Figure 1.4: A visualisation of C, P and CP symmetries and how they affect the relationship between the scattering amplitudes Γ_i.

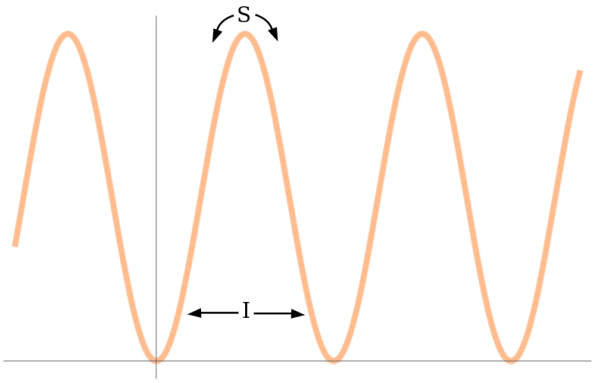

Figure 1.5: The difference between instantons and sphalerons. The barrier separates the different vacua. The sphaleron (S) goes over the top of the barrier but instantons (I) tunnel. Picture redrawn from Ref. [28].

The initial conditions for EWBG to happen are the same as for the phase transition [24]. We need a hot radiation-dominated universe where the baryon number is initially zero and for the electroweak symmetry to break and generate bubbles of false vacuum. Baryogenesis then takes place near the bubble walls, see Fig. 1.6.

We start by scattering particles from the bubble walls. In order for the CP asymmetries in the number density to be present, the scattering particles need to experience a CP and C violation. The asymmetries then bias the sphaleron transitions to produce more baryons. Some of these baryons are swept into the broken phase as the bubble wall expands, the rest diffuse to the symmetric phase. The bubble walls rapidly expanding in the plasma break the thermal equilibrium.

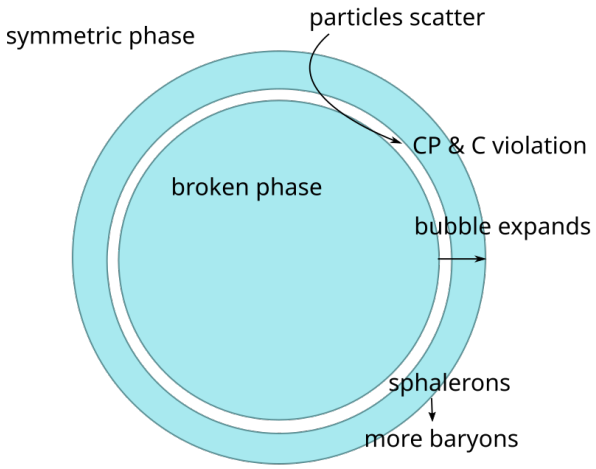

Figure 1.6: Asymmetries are created when particles scatter from the bubble wall. This creates bias, and the sphalerons produce more baryons. As the bubble expands the particles created via the sphaleron transitions get caught up by the bubble wall.

However, EWBG is not enough to explain the baryon asymmetry alone. The constraint for SM baryogenesis at the electroweak scale is the same as for the gravitational waves, the Higgs mass being too high for a first order transition to happen. Even in the case where the transition would be of first order in the SM it is not quite enough to generate a working baryogenesis scenario [24]. As with the GWs, we need to look for beyond the SM theories. For this BSM scenario to work we would need to find new particles around the electroweak scale, which makes the EWBG an attractive topic, since they could be discovered in the near future by particle colliders and other experiments.

1.3 Nucleating bubbles: non-equilibrium thermal field theory

Traditionally, bubble nucleation rate calculations have been done perturbatively. However, at large temperatures perturbation theory suffers from the so-called infrared problem [19]. This prevents us from accurately determining certain parameters that are crucial for the calculation of the rate. To achieve more precise results we must use nonperturbative approaches.

The non-perturbative approach is to discretise the four-dimensional theory on the lattice and evaluate the nucleation rate via a mix of different Monte Carlo integration methods. However, for EWPT we can actually work with the three-dimensional effective theory since at high T we can utilise the so called high temperature dimensional reduction to derive the effective theory [29]. This can be done physically because the 4D theory can be written in terms of the 3D Matsubara modes. At high T the only contributing modes are the bosonic zero modes [30].

In Fig. 1.7 we can see what the phase diagram for the SM looks like before and after the dimensional reduction. For the SM we can reduce the theory to just two dimensionless parameters x and y that depend on the coupling constants g, λ_3 and m_3. After the dimensional reduction the phase diagram can be written in the terms of x and y.

It should be noted, that perturbation theory runs into problems with gauge dependent theories [31]. Simulations, while computationally costly, could also offer a new window of possibilities for these theories. However, in the context of this thesis we do not consider gauge-dependent theories, so this is not an issue we need worry about.

We will discuss two toy models in this thesis, and while they do not include all the field content of the SM they embody the physics that many currently studied extensions, which exhibit PTs, contain. One such model is the ΣSM model [32]. As stated before, we are interested in the bubble nucleation rate as its accurate calculation is crucial when evaluating GW power spectra. The goal of this thesis is therefore to investigate the reliability of widely used perturbation theory.

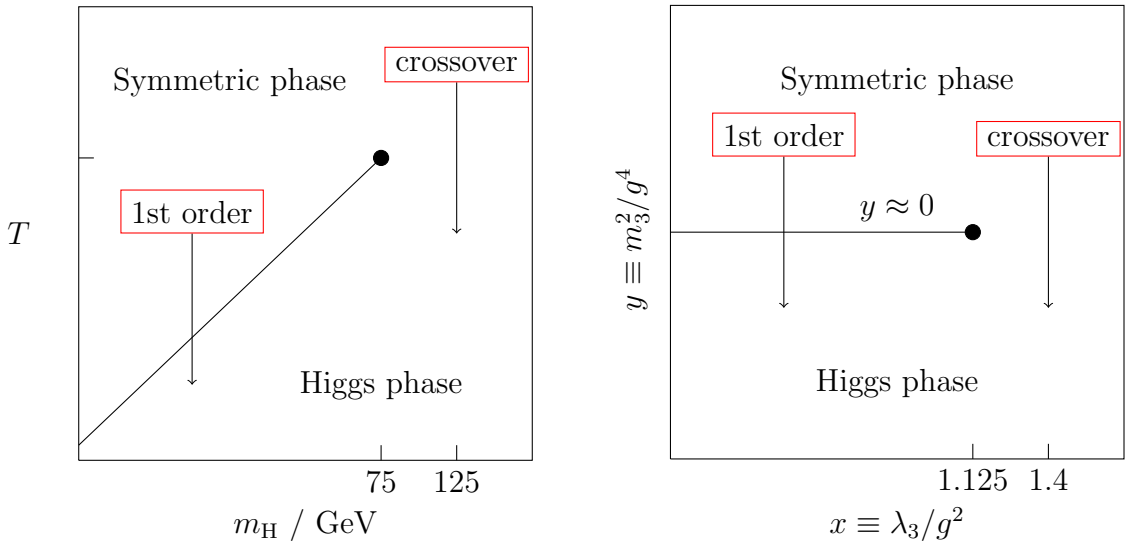

Figure 1.7: The phase diagram for the SM, before and after dimensional reduction. By the Higgs phase we refer to the broken phase. The SM can be reduced to just two dimensionless parameters x and y. Note how for example 125 GeV maps to the value $x = 1.4$. Image credit: David Weir.

Chapter 2

Bubble nucleation and tunneling

The modern approach to calculating the bubble nucleation rate from first order PTs was first introduced by Langer [33, 34]. It was then further developed by Callan and Coleman to calculate the nucleation rate in relativistic field theory [35, 36]. The nonperturbative approach was developed later largely by Moore and Rummukainen at the turn of the millennium [37, 38] and we will discuss this nonperturbative approach in later chapters.

The aim of this chapter is to briefly go through the bounce solution, starting from quantum mechanics and then eventually generalising this to finite temperature quantum field theory. We will show the analytical calculation needed to determine the nucleation rate in these finite temperatures. But first, we need to start with the bounce solution. All the following four sections rely heavily on Refs. [12, 35, 36, 39], see them for more detailed calculations of the nucleation rate. The lattice approach that we have chosen will go beyond this and is more reliable, since the bounce formalism relies on perturbation theory, and the semiclassical approximation (small $\hbar$-limit). Note that the perturbative approach works well for the zero temperature case but not for the finite temperature case since perturbation breaks down at high temperatures.

2.1 The bounce solution

The idea behind this calculation is to find the the tunneling rate Γ that depends on the detailed form of the potential. We start by looking at a particle of mass $m = 1$ that has a Hamiltonian with one degree of freedom q.

The system has a Hamiltonian of the form

$$H = \frac{1}{2}\dot{q}^2 + V(q). \tag{2.1}$$

The potential is

$$V(q) = \frac{1}{2}\omega^2 q^2 + \frac{1}{2}gq^4, \tag{2.2}$$

where g is the coupling constant and ω can be thought as the frequency of a harmonic oscillator.

The definition of the thermal partition function at some $T = 1/\beta$ when integrating over all trajectories with $-\beta/2 \leq t \leq \beta/2$ is

$$Z = \mathrm{Tr}\ e^{-\beta H/\hbar} = \sum_q \langle q|\, e^{-\beta H}\, |q\rangle = \int_{q(-\beta/2)=q(\beta/2)} \mathcal{D}q\ e^{-S_E/\hbar}, \tag{2.3}$$

where the Euclidean action with only one degree of freedom is

$$S_E = \int_{-\beta/2}^{\beta/2} dt\ \frac{1}{2}\dot{q}^2 + V(q). \tag{2.4}$$

We can show that this is equivalent to a quantum mechanical approach of calculating a transition amplitude and setting the initial and final states to be the same. To show this quantum mechanical derivation, we will look at the amplitude A for evolving between states $|q_i(t_i)\rangle$and $|q_f(t_f)\rangle$. For the details of the following calculation see Ref. [40]. We will start from the path integral formulation of A, that in the non-relativistic limit is given by

$$A = \langle q_f | \, e^{-iH(t_f - t_i)} \, | q_i \rangle = \int_{q_i}^{q_f} \mathcal{D}p\mathcal{D}q \, \exp\left(\frac{i}{\hbar} \int_{t_i}^{t_f} dt [p\dot{q} - H(p,q)] \right). \tag{2.5}$$

Now we only have one degree of freedom q, so the previous equation reduces to

$$\langle q_f | \, e^{-iH(t_f - t_i)} \, | q_i \rangle = \int_{q_i}^{q_f} \mathcal{D}q \; e^{iS/\hbar}, \tag{2.6}$$

where $S = \int_{t_i}^{t_f} L(q, \dot{q})$ and $L = \frac{1}{2}\dot{q} - V(q)$.

The above result contains the action in Minkowski space, to make things easier for us we want to rotate the system to Euclidean space $t \to -it$. Now we can see that $S \to iS_E$ and $e^{iHt} \to e^{-Ht}$. Therefore, we can now express Eq. (2.6) as

$$\langle q_f | \, e^{-\beta H} \, | q_i \rangle = \int_{q_i}^{q_f} \mathcal{D}q \; e^{-S_E/\hbar}, \tag{2.7}$$

where we have replaced $\beta = t_f - t_i$.

We now set $q_i = q_f = q$ and sum over all the possible trajectories $q(t)$ in the time range $-\beta/2 \leq t \leq \beta/2$. As we can see, we have acquired the same form as in Eq. (2.3).

The ground state energy E_0 for this system can be determined, since at large β the leading order term is E_0, thus Eq. (2.3) is dominated[1] by E_0. We can then write Tr $e^{-\beta H/\hbar} \approx e^{-\beta E_0/\hbar}$ and calculate the energy as

$$E_0(g) = -\lim_{\beta \to \infty} \frac{\hbar}{\beta} \log \int_{q(-\beta/2)=q(\beta/2)} \mathcal{D}q \; e^{-S_E/\hbar}. \tag{2.8}$$

For $g > 0$, this is a harmonic oscillator with angular frequency ω and some anharmonic corrections. However, for $g < 0$ the situation becomes complicated and an analytical

[1]Remember that the partition function can be defined via the energy eigenstates $Z = \sum_n \exp(-\beta E_n/\hbar)$.

continuation is needed to determine the ground state energy. The evaluation of the ground state energy is needed to determine the tunneling rate. This leads to E_0 having an imaginary part and the wave function thus takes the following form

$$\Psi(t) \propto e^{-i\mathrm{Re}(E_0)t - \mathrm{Im}(E_0)t}. \tag{2.9}$$

The path integral from Eq. (2.8) can now be calculated using the semiclassical approximation, where we have the classical solution and then some quantum fluctuations φ around it. Thus, we can now write

$$q(t) = q_{\mathrm{cl}}(t) + \hbar^{1/2} \underbrace{\sum_n \xi_n \varphi_n(t)}_{\varphi(t)}, \tag{2.10}$$

where we have expanded $\varphi(t)$ and ξ_n are some coefficients. Moreover, the φ_n are orthogonal and vanish at the borders, so that

$$\langle \varphi_n | \varphi_m \rangle = \delta_{nm} u_n, \tag{2.11}$$

where u_n are the norms of the normal modes[2].

We will also need the path integral measure

$$\mathcal{D}\varphi = N \prod_n \sqrt{\frac{u_n}{2\pi\hbar}} d\xi_n, \tag{2.12}$$

where N is the normalisation constant.

Next we take the variational derivative of the action with respect to the stationary point q_{cl},

[2]Since the system can be thought as of a harmonic oscillator we refer to the eigenvectors φ_n as normal modes.

$$\frac{\delta S_E}{\delta q_{cl}} = -\ddot{q} + V'(q_{cl}) = 0. \tag{2.13}$$

The second variational derivative then yields

$$\frac{\delta S_E}{\delta q(t_1)\delta q_(t_2)} = \left[-\frac{d^2}{dt^2} + V''(q_{cl})\right]\delta(t_1 - t_2). \tag{2.14}$$

However, here we want to write it conveniently in the operator form so that

$$\left[-\frac{d^2}{dt^2} + V''(q_{cl})\right]\varphi_n = \lambda_n \varphi_n, \tag{2.15}$$

where we define that the φ_n are eigenfunctions of this second derivative operator and λ_n the eigenvalues[3].

We can now determine the path integral by using the saddle point method and start by expanding the action as a series

$$\begin{aligned} S_E/\hbar &= S_E(q_{cl})/\hbar + \int dt\ \frac{\delta S_E}{\delta q}\frac{q(t) - q_{cl}(t)}{\hbar} \\ &+ \frac{1}{2}\int dt_1 dt_2\ \frac{\delta S_E}{\delta q(t_1)\delta q_(t_2)}\frac{(q(t_1) - q_{cl}(t_1))(q(t_2) - q_{cl}(t_2))}{\hbar} + ... \end{aligned} \tag{2.16}$$

The linear term in the expansion gives zero, so the path integral now becomes [4]

$$\begin{aligned} I \equiv \int \mathcal{D}q\ e^{-S_E/\hbar} &= e^{-S_E(q_{cl})/\hbar} \\ &\times \frac{1}{2}\int \mathcal{D}q\ \exp\left[-\frac{1}{2}\int dt_1 dt_2 \frac{\delta S_E}{\delta q(t_1)\delta q_(t_2)}\varphi(t_1)\varphi(t_2)\right] \\ &= e^{-S_E(q_{cl})/\hbar}\int \mathcal{D}\varphi\ \exp\left[-\frac{1}{2}\int dt \sum_n \sum_m \varphi_n \varphi_m \lambda_m \xi_n \xi_m\right] \end{aligned} \tag{2.17}$$

[3] This is essentially a harmonic oscillator at every x

[4] Note that when we change the path integral measure from q to φ we would have a factor of infinite $\hbar^{1/2}$ on the front of the integral. We neglect it since it will disappear in the end due to normalisation.

We now impose the orthogonality condition from Eq. (2.11) to get

$$I = e^{-S_E(q_{cl})/\hbar} \int N \prod_n \sqrt{\frac{u_n}{2\pi\hbar}} d\xi_n \ \exp\left[-\frac{1}{2}\sum_n \lambda_n u_n \xi_n^2\right]. \tag{2.18}$$

The integral is now just a product of Gaussians, which leads us to

$$I = e^{-S_E(q_{cl})/\hbar} N \prod_n \lambda_n^{-1/2}. \tag{2.19}$$

Thus, in the semiclassical approximation the path integral simply reduces to

$$\text{Tr } e^{H\beta/\hbar} \propto e^{-S[q_{cl}]/\hbar} \det\left(-\partial_t^2 + V''(q_{cl})\right)^{-1/2}. \tag{2.20}$$

Here we have assumed that all the eigenvalues are positive and contribute to the real part of E_0. The non-trivial part is to show that there exists exactly one negative eigenvalue for the determinant which then contributes to the imaginary part of E_0, see Ref. [41] for a detailed proof.

The equation of motion (EOM) derived from the Euclidean action in Eq. (2.13) is naturally the first variational derivative

$$V'(q) - \ddot{q} = 0. \tag{2.21}$$

The first non-trivial solution for this EOM is a constant of motion

$$E = \frac{1}{2}\dot{q}_{cl}^2 - V(q_{cl}). \tag{2.22}$$

We will now look at behaviour where, if we start from a peak of the potential, we will slide down the hill at $t = -\beta/2$ and then bounce back from the potential wall to where we started from at time $t = \beta/2$, see Fig. 2.1. Now if we take the limit $\beta \to \infty$ so that the particle starts its journey at $t = -\infty$ and returns to the original position at $t = \infty$ we have a case where $E \to 0$.

Now looking back at the EOM we can see that

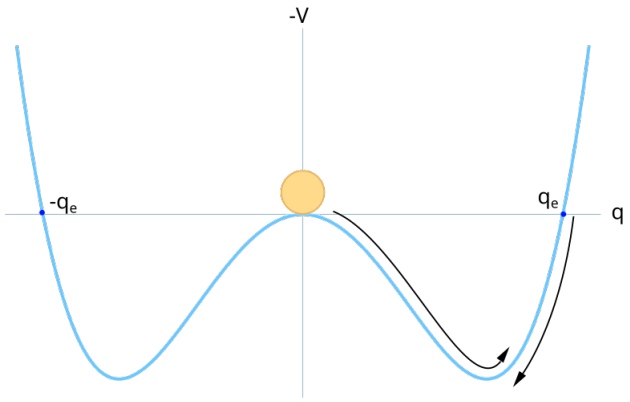

Figure 2.1: The potential $-V(q)$ for $g < 0$, q_e is the edge where the bounce back happens.

$$t = t_0 + \int_0^q dq\ (2V)^{-1/2}, \tag{2.23}$$

and we have a whole family of solutions that depend on the integration constant t_0[5].

Since the bounce has $E = 0$, for the classical action we now simply have

$$S_b = \int_{-\infty}^{\infty} dt\ \dot{q}_{cl}^2. \tag{2.24}$$

The zero mode[6] is simply the classical solution and is also an eigenvector of Eq. (2.15)

$$\frac{d}{dt}\left[-\ddot{q_{\rm cl}} + V'(q_{\rm cl})\right] = 0. \tag{2.25}$$

In fact, Eq. (2.15) has suspiciously similar form to a Hamiltonian operator of a harmonic oscillator. This helps us to draw some conclusions, first being that the zero mode corresponds to a particle bouncing back from q_e, see Fig. 2.1. This tells us that it is the first

[5]Also referred to as the collective coordinate in Ref. [12].
[6]Eigenvector with zero as an eigenvalue.

excited state of the system. This leaves us with only one possible lower energy state, and thus we only have one possible negative eigenvalue $\lambda_n < 0$, corresponding to the ground state.

Finally, we only have a few steps to do before we can give an expression for the tunneling rate. First, the integration over the zero mode has to be done and it is a rather complicated matter. It will not be shown here, see Ref. [12] for an in-depth explanation. The second thing to note is that we do not just have one singular bounce but multiple where we bounce back and forth several times. Thus, we have an exponential of the one-bounce contribution.

The energy as mentioned before has an imaginary component that allows the decay with time. We can then conclude with the probability of transitioning from one state to another

$$P_{\varphi_0 \to \text{elsewhere}} = 1 - P_{\varphi_0 \to \varphi} = 1 - e^{-2\text{Im}(E_0)t} \simeq 2\ \text{Im}(E_0)t. \tag{2.26}$$

The tunneling rate is given by

$$\Gamma = 2\ \text{Im}(E_0) = Ce^{-S_b}, \tag{2.27}$$

where C is a proportionality constant

$$C = \left(\frac{S_b}{2\pi}\right)^2 \left|\frac{\det'[-\partial_t^2 + V''(q_{cl})]}{\det[-\partial_t^2 + V''(0)]}\right|, \tag{2.28}$$

where $\det'$ marks the omission of zero modes in the determinant.

This is intended as a short summary of the calculation and omits some crucial steps. For more information on the calculation see Refs. [12, 35, 36, 39].

2.2 Tunneling at zero temperature

We will now look at the bounce solution for zero temperature case. This is quantum mechanical in nature and we can reduce it to a three dimensional effective theory. We start with a scalar field theory with the action

$$S_M = \int dt\ dx^3 \left[\frac{1}{2}\dot{\phi}^2 - \frac{1}{2}(\nabla\phi)^2 - V(\phi)\right]. \tag{2.29}$$

As in the one-dimensional case, because this is the action in Minkowski space we need to do a Wick rotation to move into the Euclidean space. In other words, we replace time by imaginary time $\tau = it$. One of the reasons why we want to perform this rotation to the Euclidean space is that the causal structure of the Minkowski space is more complicated and performing calculations in the Euclidean space is easier. The Euclidean action takes the following form

$$S_E = \int d\tau\ dx^3 \left[\frac{1}{2}\left(\frac{d\phi}{d\tau}\right)^2 + \frac{1}{2}(\nabla\phi)^2 + V(\phi)\right] \tag{2.30}$$

We impose the following boundary conditions on the system

$$\lim_{\tau\to\pm\infty} \phi(\tau, x) = 0 \quad \text{and} \lim_{x\to\infty} \phi(\tau, x) = 0 \tag{2.31}$$

We assume that the bounce has an O(4) symmetry. We can now move to radial coordinates where $r = (\tau^2+x^2+y^2+z^2)^{1/2}$ and the integration measure is now the volume of a 4-sphere $dx^4 = 2\pi^2 r^3 dr$. The Euclidean action from Eq. (2.30) becomes

$$S_E = 2\pi^2 \int_0^\infty dr\ r^3 \left[\frac{1}{2}\left(\frac{d\phi}{dr}\right)^2 + V(\phi)\right]. \tag{2.32}$$

This now becomes the S_b in Eq. 2.27 and we are left with determining the dreaded determinant in the same equation. The determinant is generally the most complex part of

the calculation, but it also contains the dynamical information of the system.

Since the exponential dependence of the action, we can simply minimise the it to get the dominant contribution. Now we can easily solve the equation of motion to be

$$\frac{d^2\phi}{dr^2} + \frac{3}{r}\frac{d\phi}{dr} - V'(\phi) = 0, \tag{2.33}$$

where the boundary conditions are now $\lim_{r\to\infty}\phi(r) = 0$ and $\frac{d\phi}{dr}|_{r=0} = 0$.

For zero temperature there are four zero modes. Hence the proportionality constant becomes

$$C = \left(\frac{S_E}{2\pi}\right)^2 \left|\frac{\det'[-\partial^2 + V''(\phi_b)]}{\det[-\partial^2 + V''(0)]}\right|^{-1/2}, \tag{2.34}$$

where ϕ_b is the bounce solution that can be determined using the EOM.

2.3 Tunneling at finite temperature

The last step is to finally generalise all we have done thus far to finite temperatures. We now replace the potential $V(\phi)$ by the effective potential $V(\phi, T)$ that depends on the temperature. It has the same shape as the potential in Fig. 1.2, so that at temperature T_c and lower it will have two minima. The action is

$$S_4 = \int_0^{1/T} d\tau \int dx^3 \left[\frac{1}{2}(\partial_\mu\phi)^2 + V(\phi, T)\right]. \tag{2.35}$$

Since the action is now periodic in $1/T$, we can see that in the limit $T \to 0$ things would reduce back to the zero temperature behaviour. However, the limit $T \gg \frac{1}{R}$ is the important one here, since in that limit the dependence ϕ has on time becomes zero [42], see

Fig. 2.2.

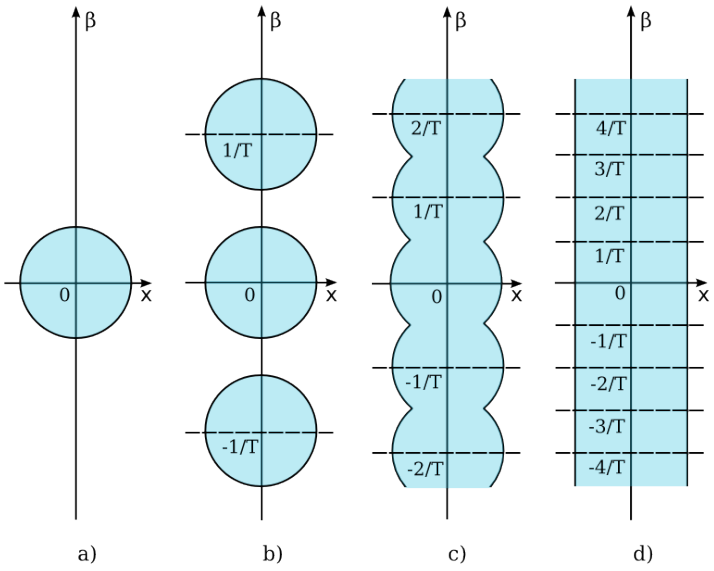

Figure 2.2: a) $T = 0$, b) $T \ll 1/R$, c) $T \approx 1/R$, d) $T \gg 1/R$, coloured regions contain a classical scalar field ϕ. In the limit $T \gg 1/R$ the dependency that ϕ has on T becomes zero. Redrawn from Ref. [42].

Hence we can just integrate out the time dependence and the action becomes

$$S_4 = \frac{S_3}{T}, \tag{2.36}$$

where

$$S_3 = \int dx^3 \left[\frac{1}{2}(\nabla\phi)^2 + V(\phi, T)\right]. \tag{2.37}$$

We now have an O(3) symmetry at reasonably high T. Again we move to spherically symmetric coordinates where $r = \sqrt{x^2 + y^2 + z^2}$ and the action reads

$$S_3 = 4\pi \int_0^\infty dr\ r^2 \left[\frac{1}{2}\left(\frac{d\phi}{dr}\right)^2 + V(\phi, T)\right]. \tag{2.38}$$

The equation of motion (bounce equation) now takes a very similar form

$$\frac{d^2\phi}{dr^2} + \frac{2}{r}\frac{d\phi}{dr} - V'(\phi, T) = 0, \tag{2.39}$$

and it has the following boundary conditions $\lim_{r\to\infty}\phi(r) = 0$ and $\frac{d\phi}{dr}|_{r=0} = 0$.

There are now three contributing zero modes, from the three spatial dimensions and they contribute to the prefactor as $[S_4/(2\pi)]^{3/2} = [S_3/(2\pi T)]^{3/2}$. The prefactor is now[7]

$$C = \frac{\kappa}{\pi}\left(\frac{S_3}{2\pi T}\right)^{3/2}\left|\frac{\det'[-\nabla^2 + V''(\phi)]}{\det[-\nabla^2 + V''(0)]}\right|^{-1/2}. \tag{2.40}$$

See Ref. [12] for further discussion on the calculation of the determinant.

2.4 Thin-wall approximation

Finally, we consider a solution to the bounce equation (2.39), namely the thin-wall approximation. The thin-wall approximation only holds when the energy difference between the symmetric and broken phase is small compared to the height of the potential barrier. In this approximation the tunneling rate is also relatively small. Fig. 2.3 represents the profile of a vacuum bubble. It consists of two parts, the interior region where $\phi = \phi_0$ and the bubble wall. The constant part is the volume energy that is the result of tunneling to the true vacuum. The bubble wall is the surface tension between the true and broken vacua. Outside the bubble the action is zero such that $\phi \approx 0$ and $V(\phi) \approx 0$.

At this limit the action from Eq. (2.37) can be integrated in two parts. The first part involving the potential becomes

[7]Notice the κ/π factor, it differs from the zero temperature case and can be thought as of a dynamical part of the prefactor.

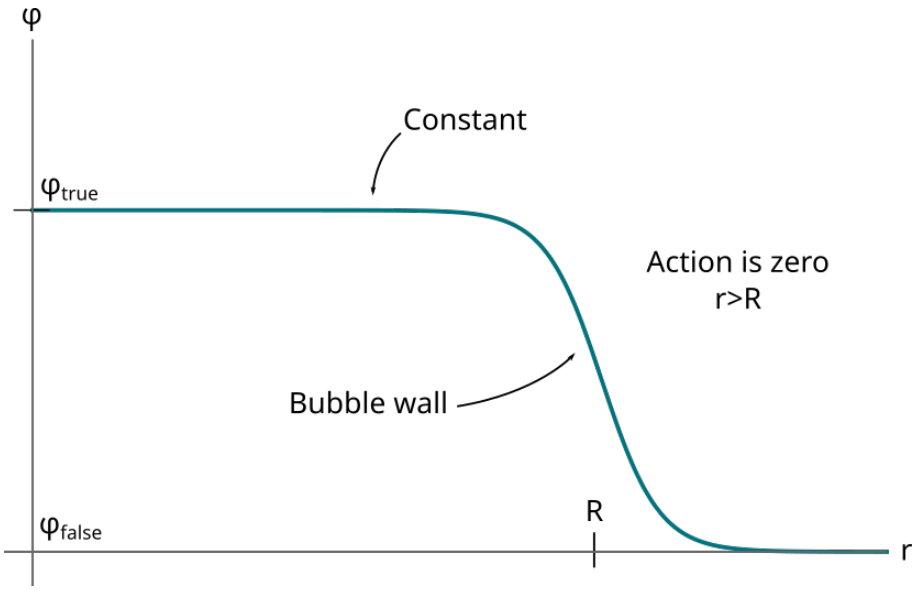

Figure 2.3: The bubble profile in the thin-wall approximation. The φ_{true} and φ_{false} signify the broken and symmetric phases. When $r < R$ the solution φ is a constant, where R is the size of the bubble. Outside the bubble $\varphi \approx 0$.

$$4\pi \int_0^R dr\ r^2 V(\phi, T) = \frac{4\pi R^3}{3} V(\phi_0, T), \tag{2.41}$$

where $V(\phi_0, T) < 0$ so it is more convenient to write it as $-|\bar{V}(T)|$.

The second part of the integral is proportional to $(d\phi/dr)^2$. From the Fig. 2.3 we can see that the derivative $d\phi/dr$ is going to be peaked at $r = R$. The only meaningful contribution when we integrate over r is then going to be from the derivative and we can pull the r^2 outside the integral. Thus, we can write

$$4\pi R^2 \int_0^\infty dr \frac{1}{2} \left(\frac{d\phi}{dr}\right)^2 = 4\pi R^2 S_1(T). \tag{2.42}$$

Hence, in the thin-wall approximation the Euclidean action is simply

$$S_3(R) = -\frac{4\pi R^3}{3}|\bar{V}(T)| + 4\pi R^2 S_1(T). \tag{2.43}$$

The approximate solution to the bounce equation is therefore acquired just by minimising this action and can be written as

$$R(T) = \frac{2S_1(T)}{|\bar{V}(T)|}. \tag{2.44}$$

When applying the thin-wall approximation on the cubic anisotropy model we will use slightly different notation. First, let us define ϵ as the difference between the symmetric and broken phase, namely the height of the potential barrier (see Fig. 2.4)

$$\epsilon = V_{\text{sym}} - V_{\text{broken}}. \tag{2.45}$$

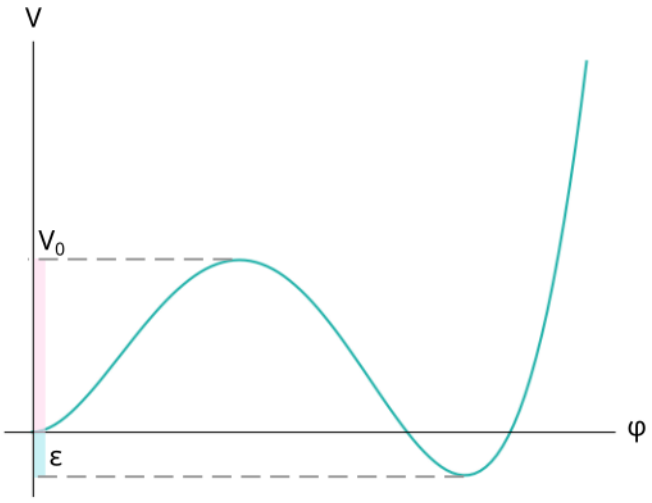

Figure 2.4: Example of a potential that would be appropriate for the approximation, where V_0 is the height of the potential barrier. For the thin-wall approximation the height of the potential barrier must be larger than the energy difference between the broken and symmetric phase, $\epsilon/V_0 \ll 1$.

Now the action can be written as

$$S = -\frac{4\pi}{3}R^3\epsilon + 4\pi R^2 S_1, \tag{2.46}$$

where now minimising this we get $R = 2S_1/\epsilon$ as above. Finally, after minimising the action we can write it as

$$S_3 = \frac{16\pi S_1^3}{3\epsilon^2}. \tag{2.47}$$

Hence we can see that the tunneling rate indeed is small if we consider $\Gamma \sim e^{S_3/T}$, including the determinant part again complicates things further. Usually, the prefactor can be approximated by $\sim m^4$.

Chapter 3

Gravitational waves

Gravitational waves are ripples in spacetime. GWs are one of the predictions of Einstein's theory of General Relativity (GR) and ever since the proposal in 1916 physicists have been looking for them. Like mentioned earlier, they were finally detected almost exactly 100 years later in 2016 by LIGO and Virgo [3]. GWs provide a unique window to the physics of the early universe that would be otherwise unreachable. In our case, we are interested in so called stochastic GW background (SGWB), relic GWs from the very early universe that could still be detectable. These GWs would have produced a continuous signal, much like the Cosmic Microwave Background (CMB) [43]. One source of these GWs are first order PTs, and the future space-based GW detector LISA would be in the optimal frequency range for their detection [6]. For a review on GWs from first order PTs see Ref. [44]. In this chapter we will: 1) look at how one would proceed from a theory to a GW power spectrum and finally to a signal-to-noise ratio (SNR) estimate for LISA and 2) the different processes of generating GWs that contribute, depending on the model. One should note that the models we are discussing later in Chapters 6 and 7 are toy models and while they can be used to study the nucleation rate, they are not valid for simulating GW spectra for the EWPT.

We will adopt the following convention for the subsequent sections. Parameters marked with $*$ happen at T_*, which is the temperature of the thermal bath at time t_* when the bubbles are nucleated. The parameter α is the transition strength, β the inverse time duration of the PT, H_* the Hubble parameter. The bubble wall velocity is denoted by v_w and g_* is the number of relativistic degrees of freedom. The parameter κ_ϕ tells the

fraction of latent heat that is converted into the kinetic energy of the field. Similarly, κ_v is the fraction converted into bulk motion of the fluid.

3.1 LISA and GWs from first order phase transition

The first thing to do when starting to determine if a certain particle physics model could be detectable by LISA is to write out the field content and Lagrangian of the theory. The next step is to find the effective theory and whether it has a first order transition or not. Next we need to compute H_* and β, using the bubble nucleation rate. This is the part of the pipeline we are working on, namely the first arrow in the Fig. 3.1. After determining PT parameters we can achieve a GW power spectrum for the theory. Then depending on the LISA sensitivity, we can see whether or not a signal could be detectable [45].

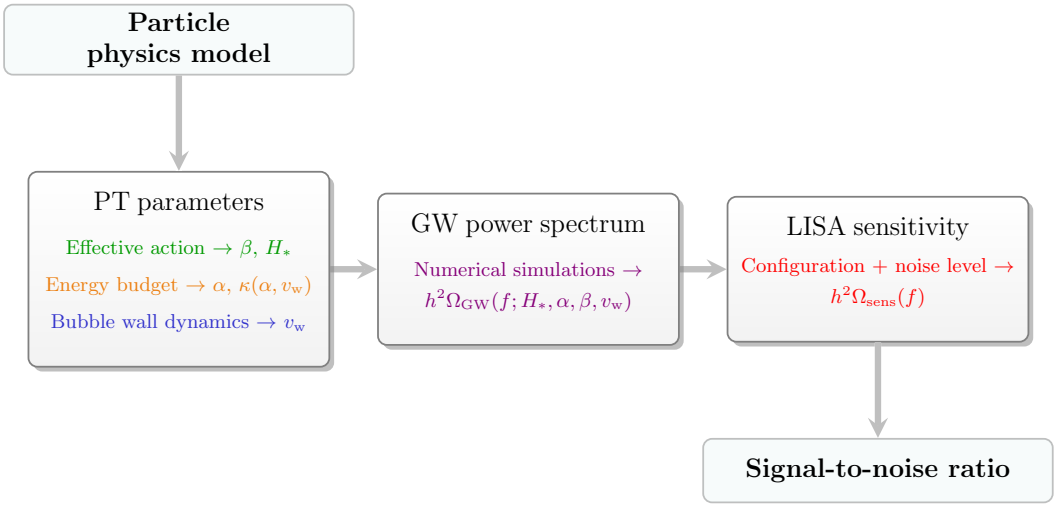

Figure 3.1: The LISA pipeline describes how one would proceed from a particle physics model all the way to the SNR for LISA. Image from Ref. [45].

The calculation of the nucleation rate that was shown perturbatively in Chapter 2 is crucial for solving β, since the relationship between the nucleation rate and the inverse duration of the PT is

$$\beta(T) = \frac{d}{dt} \ln \Gamma(T). \tag{3.1}$$

As stated before, the cubic anisotropy model and the real scalar theory that we are looking at later in more detail are toy models. When speaking of the different gravitational wave contributions they do not correspond to the different GW contributions introduced in the next section. However, the cubic anisotropy model is similar to the qualitative features of the minimal SM which for the dominant contribution can be thought of as a thermal (sound) transition. We would like to emphasise that the contributions of the next section highly depend on the model in question. However, they offer us crucial information on the general nature of these kind of PTs and the dynamics behind them.

3.2 GW production

The GW background from PTs has three main processes that produce GWs, the importance of a contribution from a certain process depends on the model in question. The contributions are from bubble wall collisions Ω_ϕ, when the initial collisions of the scalar field shells happens, the sound waves in the plasma Ω_{sw} as the kinetic energy keeps propagating and magnetohydrodynamic (MHD) turbulence Ω_{turb}. The total contribution can be written as

$$h^2\Omega_{\text{GW}} \simeq h^2\Omega_\phi + h^2\Omega_{\text{sw}} + h^2\Omega_{\text{turb}}. \tag{3.2}$$

Please note that this is also an approximation. We will now briefly introduce each contribution.

3.2.1 Collisions

As stated before, the bubbles colliding with each other produce GWs. The estimation of this contribution is traditionally done with the envelope approximation, since it is easier to do than using the Klein-Gordon equation for the evolution of the scalar fields. This contribution is dominant for vacuum transitions, where the effects of the surrounding plasma are negligible or when the transition is strong i.e. $\alpha \gg 1$ [11].

The envelope approximation neglects the bubble overlap areas and their interactions and is only concerned with the colliding bubble walls, see Fig. 3.2. The approximation makes the calculation less demanding and is reasonably accurate in its predictions [46]. However, in the light of recent numerical simulations and their results, it seems that the envelope approximation is not as accurate as was previously thought to be the case [47].

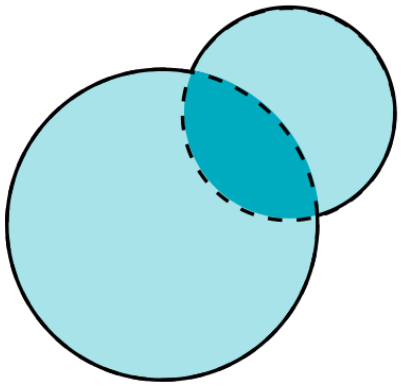

Figure 3.2: The envelope approximation. The dark blue are is the overlap region that is neglected, instead only the bubble walls are accounted for.

We can write the gravitational wave power spectrum for the bubble wall collisions as [48, 49]

$$
\begin{aligned}
h^2\Omega_\phi(f) &= 1.67\times10^{-5}\left(\frac{H_*}{\beta}\right)^2\left(\frac{\kappa_\phi\alpha}{1+\alpha}\right)^2 \\
&\times \left(\frac{100}{g_*}\right)^{1/3}\left(\frac{0.11v_w^3}{0.42+v_w^2}\right)\left(\frac{3.8(f/f_\phi)^{2.8}}{1+2.8(f/f_\phi)^{3.8}}\right).
\end{aligned}
\tag{3.3}
$$

The peak frequency f_* is

$$
\frac{f_*}{\beta} = \frac{0.62}{1.8-0.1v_w+v_w^2}
\tag{3.4}
$$

and when redshifted to today

$$
f_\phi = 1.65\times10^{-2}\text{mHz}\left(\frac{f_*}{\beta}\right)\left(\frac{\beta}{H_*}\right)\left(\frac{T_*}{100\text{GeV}}\right)\left(\frac{g_*}{100}\right)^{1/6}.
\tag{3.5}
$$

3.2.2 Sound waves

The collision of the bubbles last a relatively short period of time. A more significant source of GWs comes from the sounds waves that are created as bubbles move in the plasma. Since the envelope approximation only accounts for the bubble walls, it fails to take this contribution into account. Furthermore, like the turbulence, the sound waves are present even after the PT has finished. This makes the sound wave contribution more significant than the one from the envelope approximation [12].

The sound wave contribution is

$$
\begin{aligned}
h^2\Omega_{\text{sw}}(f) &= 2.65\times10^{-6}\left(\frac{H_*}{\beta}\right)\left(\frac{\kappa_v\alpha}{1+\alpha}\right)^2 \\
&\times \left(\frac{100}{g_*}\right)^{1/3} v_w\left(\frac{f}{f_{\text{sw}}}\right)^3\left(\frac{7}{4+3(f/f_{\text{sw}})}\right)^{7/2},
\end{aligned}
\tag{3.6}
$$

where again the peak frequency after redshifting is given by

$$f_{\rm sw} = 1.9 \times 10^{-2}{\rm mHz}\frac{1}{v_w}\left(\frac{\beta}{H_*}\right)\left(\frac{T_*}{100{\rm GeV}}\right)\left(\frac{g_*}{100}\right)^{1/6} \tag{3.7}$$

Sound waves in general are thought to be the dominating contribution out of the three.

3.2.3 Turbulence

The cosmic fluid is fully ionised primordial plasma. One of its main characteristics is a high Reynolds number, which means that it can become turbulent very easily. Therefore, the colliding bubbles that inject energy to the fluid cause it to develop MHD turbulence. This is a long lasting source of GWS, since the MHD turbulence decays slowly after the PT has already ended [11].

The contribution from MHD turbulence can be written as

$$\begin{aligned} h^2\Omega_{\rm turb}(f) &= 3.35 \times 10^{-4}\left(\frac{H_*}{\beta}\right)\left(\frac{\kappa_{\rm turb}\alpha}{1+\alpha}\right)^{3/2} \\ &\times \left(\frac{100}{g_*}\right)^{1/3} v_w \frac{(f/f_{\rm turb})^3}{[1+(f/f_{\rm turb})]^{11/3}(1+8\pi f/h_*)} \end{aligned} \tag{3.8}$$

where $\kappa_{\rm turb} = \epsilon\kappa_v$ is some fraction of the bulk kinetic energy and again the redshifted peak frequency is given by

$$f_{\rm turb} = 2.7 \times 10^{-2}{\rm mHz}\frac{1}{v_w}\left(\frac{\beta}{H_*}\right)\left(\frac{T_*}{100{\rm GeV}}\right)\left(\frac{g_*}{100}\right)^{1/6}. \tag{3.9}$$

Quantifying the effect of turbulence still remains a challenge to this day. It may never even occur if the Hubble damping happens on a shorter time scale. As we saw from all the GW spectrum equations, things heavily depend on the value of β. Hence determining it accurately is of utmost importance.

3.3 Modelling the GW spectra

The accurate calculation of the parameters α, β and T_* is tricky. Perturbation theory offers a low level of accuracy and the theoretical uncertainties are large. Hence it is better to use the nonperturbative approach. The bubble wall speed v_w cannot be estimated using the methods presented in this thesis and has to be done separately.

As we can see, all above quantities are important when estimating the frequency range for LISA. If we want to use LISA, we have to minimise the uncertainty of these parameters and define the GW spectrum parameters as accurately as possible. When the thermodynamical quantities have been calculated we can get the approximate result $h^2\Omega_{\rm gw}$ and calculate the SNR defined as [7]

$$\mathrm{SNR} = \sqrt{\tau \int_{f_{\rm min}}^{f_{\rm max}} df \ \left[\frac{h^2\Omega_{\rm gw}(f)}{h^2\Omega_{\rm sens}(f)}\right]}, \tag{3.10}$$

where τ is the duration of the mission and $h^2\Omega_{\rm sens}$ the sensitivity of LISA.

In Fig. 3.3 we have plotted the sound curve, since it is thought to be the dominating one, against the sensitivity curve of LISA. The naive assumption would be that the signal would not be detectable if looking at the sensitivity curve from the sound waves. It clearly remains below the LISA sensitivity curve. However, there is a caveat to the sensitivity curves, they fail to illustrate the fact that the observation time for these missions is long. What we should look at instead when estimating the detectability of a signal are the parameter contour plots that highlight the dependence on the acquired SNR. Based on that, the parameters we have used in Fig. 3.3 could possibly be detectable in the near future.

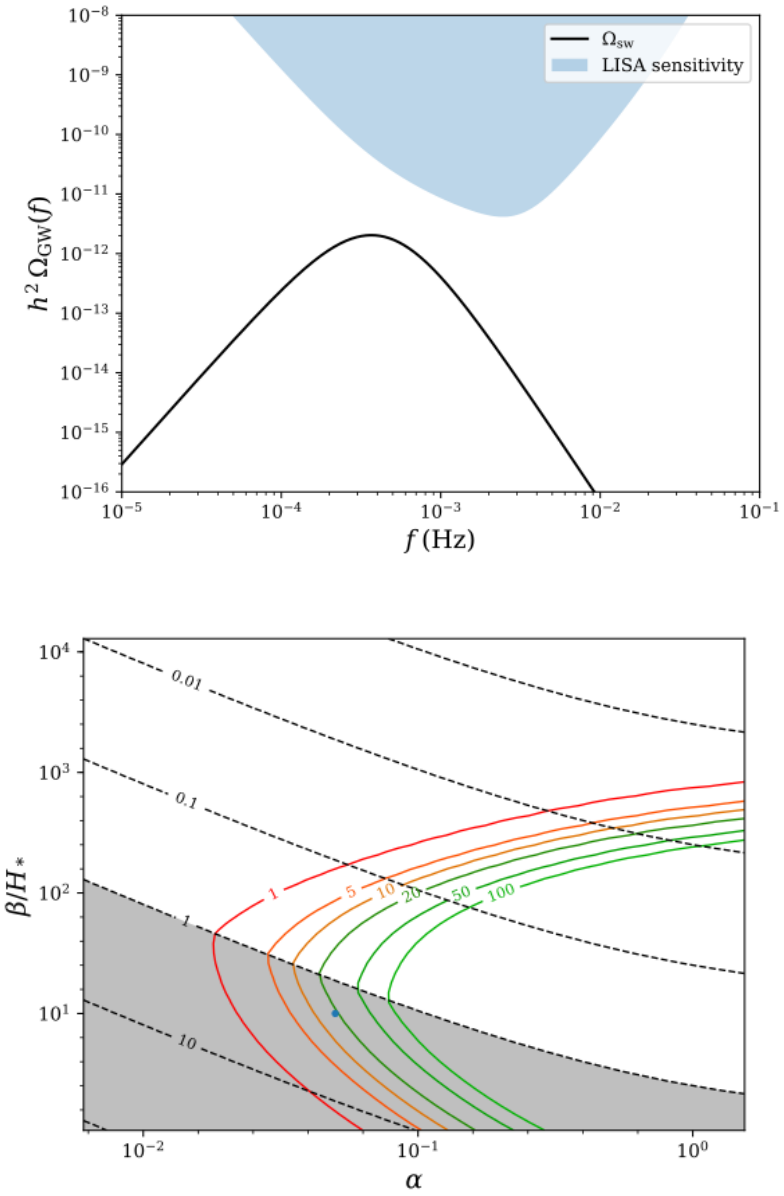

Figure 3.3: LISA sensitivity plots (top) and the parameter contour plot (bottom). The dashed line contours (black) are the amount of Hubble time to fluid turnover time. The SNR of LISA for given mission profile are the colourful contours. The parameters used are $v_w = 0.44$, $\alpha_\theta = 0.084$, $\beta/H_* = 0.1$, $T_* = 180$ GeV and $g_* = 106.75$. Image credit: David Weir.

Chapter 4

Simulation methods

Generally speaking there are two possible ways of calculating the complex bubble nucleation rate. The first is perhaps the more traditional one with perturbation theory. However, it is known to have its weaknesses when it comes to large coupling constants at high temperatures. The second option is to use lattice simulations, since they are more reliable. Here we will take a short look at the basic lattice formalism and then go through the different methods and tools we have used in the simulation code.

4.1 The lattice formalism

How do we simulate the physics of such a complex process on a computer? The short answer is to put the universe into a lattice. A lattice is very simply a finite sized box with some finite lattice spacing a, see Fig. 4.1. Lattice field theory emerged in the late 1960s and is now the standard non-perturbative method to look at high energy physics. A crystal lattice is an example of a lattice that has a physical origin behind it but in the context of this thesis, a lattice simply is an approximation of continuous fields. In the context of the EWPT, the first lattice calculations were performed around 1994 [50, 51]. For a reference on basic lattice formalism see Ref. [52].

When we move to the lattice formalism there are a couple of differences to the continuum

one. We discretise space, first the coordinates are defined as

$$\bar{x} = a\bar{n} \quad \text{where} \quad n_i \in \{0...N_i\}, \tag{4.1}$$

where N_i is the number of sites (discrete points) in the ith dimension and in total

$$N = \prod_{i=1}^{d} N_i, \tag{4.2}$$

where d is the number of dimensions. For example in three dimensions when $n_x = n_y = n_z$ the lattice is cubic, but also other configurations exist, such as the cylindrical one.

The integral measure and derivative turn to finite sums and differences[1]

$$\int dx^3 \to a^3 \sum_x \quad \text{and} \quad \partial_\mu \phi \to \frac{1}{a}[\phi_{x+\mu} - \phi_x]. \tag{4.3}$$

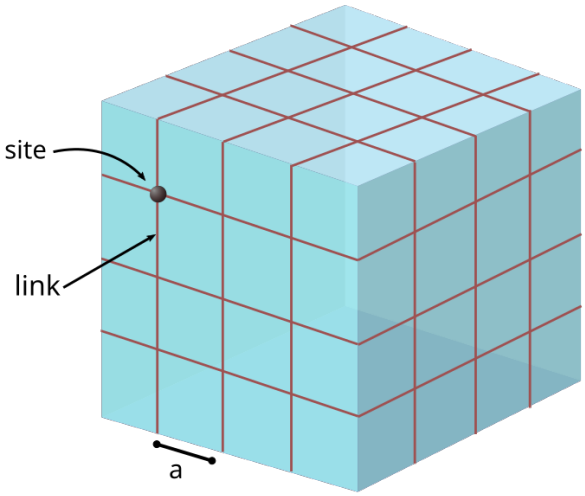

Figure 4.1: A 4^3 cubic lattice with 4^3 sites, a is the lattice spacing.

Naturally, now that we have discretised our system, the results we acquire will be different from the continuum ones. Therefore, in order to get back to the continuum results we

[1]The conversion of the derivative shown here is the lowest order, $\phi_{x+\mu}$ only takes into account the nearest neighbours, but this can be easily improved by also considering the next-to-nearest neighbours.

must take two limits, the continuum limit $a \to 0$ and the thermodynamic limit $V \to \infty$. It is also very common to use periodic boundary conditions to avoid having to deal with the edges of the box.

To illustrate how to convert between continuum and lattice equations let us take a look at a free scalar field theory. It has the following Euclidean action in the continuum

$$S_E = \int d^3x \ \left[\frac{1}{2} \partial_\mu^2 \phi + \frac{1}{2} m^2 \phi^2 \right]. \tag{4.4}$$

All the actions we use from now on are 3D ones. This is due to the fact that we perform dimensional reduction at high temperatures. This allows us to perform computations on three-dimensional effective theories.

Now if we use the Eqs. 4.3 the action will read as

$$S_L = a^3 \sum_x \left[\frac{1}{2} \sum_\mu \left(\frac{1}{a^2} (\phi_{x+\mu} - \phi_x)^2 + \frac{1}{2} m^2 \phi^2 \right) \right]. \tag{4.5}$$

We absorb the lattice spacing a into the fields and move to dimensionless lattice quantities. It is now straightforward to read off the relationship between the continuum and lattice quantities

$$\phi = a^{-1/2} \phi_L \tag{4.6}$$

$$m^2 = a^{-2} m_L^2. \tag{4.7}$$

We can now write the action in Eq. (4.5) with the help of the lattice quantities and it reduces to

$$S_L = \sum_x \left[\frac{1}{2} \sum_\mu (\phi_{x+\mu,L} - \phi_{x,L})^2 + \frac{1}{2} m_L^2 \phi_L^2 \right]. \tag{4.8}$$

One should note that the conversion to lattice action done in Eq. (4.5) is generally thought to be a naive one. However, here it is the exact one since the field theory does not have any interaction terms. Usually getting reliable results from a lattice calculation involves the use of counterterms. The purpose of these counterterms is to make the convergence at $a \to 0$ faster as well as smoother. Without them, the result would not necessarily be finite. The calculation of these counterterms can be done analytically. In Chapter 6 we will present the actions with the counterterms present in the lattice formulation.

4.2 Equilibrium lattice techniques

For the Monte Carlo methods and update algorithms see [53] for a reference.

4.2.1 Monte Carlo and Markov Chains

The Monte Carlo (MC) methods borrow their name from the famous casino located in Monaco. As their gambling counterpart MC methods also involve randomness that determine the outcome of events. It first emerged in the 40s and 50s and is generally thought to be invented by Metropolis, Rosenbluth, Ulam and von Neumann as a part of their work during the Manhattan Project [54, 55].

However, Monte Carlo is not the first time randomness has been explored as a way of evaluating physical measurements. The most famous example is perhaps the Buffon's needle that dates back all the way to year 1777 [56]. The experiment was to evaluate the value of pi by dropping needles on lines. Essentially, MC methods are a more sophisticated version of dropping needles. Nowadays, it is the standard way of doing calculations that are analytically unsolvable or too time consuming. They are utilised in many research fields, ranging from social sciences to physics [54]. There are many different MC methods one can use depending on the purpose. One subset of these are the Markov Chain Monte Carlo (MCMC) algorithms. For example, the Metropolis update is a MCMC method and we will describe it in more detail later.

In physics, Monte Carlo methods can be used to study thermodynamics of a condensed matter system or quantum field theories. We want to make use of the latter and get configurations from a thermal ensemble. The most commonly used is the canonical ensemble

$$Z = \int \mathcal{D}\phi \; e^{-H(\phi)/T} \tag{4.9}$$

More specifically, we want to know the expectation value of some observable A which in the path integral formulation is

$$\langle A \rangle = \frac{1}{Z} \int \mathcal{D}\phi \; A e^{-H(\phi)/T}. \tag{4.10}$$

The numerical evaluation of this path integral is tricky, thankfully instead of drawing samples from a uniform distribution we can now make use of the Boltzmann distribution. By drawing the samples A_i from the Boltzmann distribution we can define the expectation value of A as

$$\langle A \rangle = \frac{1}{N} \sum_i A_i, \tag{4.11}$$

where we sum over the different configurations i and divide by the total number of points N. This is called importance sampling.

Naturally, MC methods also come with their drawbacks. They can be computationally very costly, always give an approximate solution and exhibit autocorrelation behaviour, for more details on autocorrelation and error analysis see Section 4.4.2 onwards.

The update algorithms we have used fulfil the detailed balance condition

$$\frac{W_f(\phi \to \phi')}{W_f(\phi' \to \phi)} = \frac{p_{eq}(\phi')}{p_{eq}(\phi)} = e^{(H(\phi) - H(\phi'))/T}, \tag{4.12}$$

where $W_f(\phi \to \phi')$ is the transition probability of moving from phase ϕ to phase ϕ' along some trajectory and $p_{eq}(\phi)$ some stationary point.

The detailed balance simply states that in equilibrium each process is in equal to its reverse process. This allows us to determine whether we should accept the update or not.

It is not a requirement for the MC to satisfy this condition, but most algorithms do.

4.2.2 The Metropolis update

The Metropolis update is a Markov Chain MC (MCMC) and an importance sampling method used in updating the field configurations according to some probability distribution. It fulfils the detailed balance condition. The transition probability tells us whether or not we should accept the update. We use both local and global radial Metropolis updates of the Monte Carlo scheme. The local update is closest to the usual Metropolis update algorithm, with the distinction that it takes into account the multicanonical weight function. The global radial update is a bit more complicated, but the basic idea remains the same. See Ref. [57] for more details on the global radial update.

Note that here we have considered the effect of the multicanonical MC by adding the weight w to the algorithm, the multicanonical update will be discussed later. We define δH as the energy change from the proposed update.

The local update algorithm can be described as

- Choose a site you want to update.
- Draw a random number from a distribution $\phi' \in [-\delta\phi, \delta\phi]$.
- Accept the update if $\delta H - \delta w \leq 0$.
- If the above condition was not met generate a new uniform random number u that determines the probability of accepting the update. Draw a value such that $u = [0, 1)$ and accept the update if the condition $u \leq e^{-\delta H + \delta w}$ is met.

The global radial update introduces some nuances to the calculation

- Draw a random number ξ from a uniform distribution around zero $\xi \in [-\epsilon, \epsilon]$.
- This determines the radius $R = e^{\xi}$.

- Determine the sums a and b of the parts of the action that are proportional to R^2 and R^4. The change of the action will now take the form of $\delta H = (R^4 - 1)a + (R^2 - 1)b$.
- Accept update if $\delta H - \delta w - 4V\xi \leq 0$.
- If above condition is not met, proceed as in local update except that now we must fulfil the condition $u \leq \exp(-\delta H + \delta w + 4V\xi)$.

The global radial update is used to enhance the tunneling. It changes the magnitude of the whole lattice in a single step; the magnitude change in the field is involved in tunneling processes.

4.2.3 Overrelaxation

The Metropolis algorithm is a good general update but it does not change the system very much, thus we need to use overrelaxation. Overrelaxation is a good way to reduce the dependency of successive steps of the system, see discussion about autocorrelation in Section 4.4.2. However, it cannot the be used alone since it does not sample all the possible configurations. In the simulation code we use a mix of overrelaxation and Metropolis.

The algorithm assumes that there is some symmetry in the Hamiltonian in a way that $H(\phi) = H(\phi')$. For example, in the Ising model the overrelaxation algorithm would flip the up-spin to down and vice versa[2]. Think of a region surrounded many up spins and one down spin in the middle. The Metropolis update would need many iterations to change the spin inside the domain. Overrelaxation can do it in one step. However, it would also cause it to change back if used as the only method for updating the configuration. Hence one needs to use a mix of these algorithms to visit all possible states.

In our case it is not quite as simple. Simply flipping the sign of the field ϕ does not work. Instead, we look at the field at one point $\phi_{x,y,z}$ and treat the other sites and

[2]Note that this would also cause a huge change in energy, so using overrelaxation on Ising model is not the best of ideas in real life.

fields as constants. Essentially, we want to find such a ϕ' that fulfils the aforementioned $H(\phi) = H(\phi')$. How do we go about on solving an equation like this? We start by parametrising the Hamiltonian at some point (x, y, z) as

$$H(\phi) = c_0 + c_1\phi + c_2\phi^2 + c_3\phi^4. \tag{4.13}$$

This leads us to a situation where we need to solve the following equation

$$c_1 + c_2\phi' + c_3\phi'^2 + c_4\phi'^4 = c_1 + c_2\phi + c_3\phi^2 + c_4\phi^4. \tag{4.14}$$

This of course, is of fourth order and quite inconvenient for us. Thankfully, we can write it in a more convenient way and reduce it to a third order polynomial, knowing that $\phi = \phi'$ is naturally one solution to the equation. We now denote $\phi = \phi_0$ since it is just some known point of the field:

$$\phi'^3 + \phi'^2\phi_0 + \phi'\left(\phi_0^2 + \frac{c_3}{c_4}\right) + \left(\phi_0^3 + \frac{c_3}{c_4}\phi_0 + \frac{c_2}{c_4}\right) = 0 \tag{4.15}$$

We can now solve for ϕ'. As it turns out, only one real solution exists. The final step is to calculate the measure needed to satisfy the detailed balance condition

$$\frac{d\phi_0}{d\phi'} = \frac{dS(\phi')/d\phi'}{dS(\phi_0)/d\phi_0} \tag{4.16}$$

We then proceed as in Metropolis using the acquired measure as the condition for update.

- If the update is multicanonical $\frac{d\phi_0}{d\phi'} \to \frac{d\phi_0}{d\phi'}e^{\delta w}$.
- Update if $\frac{d\phi_0}{d\phi'} \to \frac{d\phi_0}{d\phi'} \geq 1$.
- If this condition is not met draw a random number $u \in (0, 1]$.
- If $\frac{d\phi_0}{d\phi'} \geq u$, accept. Otherwise reject the update.

4.2.4 Reweighting

One MC run of the simulation code provides us with measurements at one choice of the parameters. It would be a waste of resources to run a new simulation for every single mass parameter. Luckily, reweighting comes to the rescue and provides us with results for points that are sufficiently close to the original one acquired from the simulation [58]. Reweighting is also useful in the multicanonical MC update, see next section.

Start by assuming we have run a simulation and now have a probability distribution of the form

$$P_{m_1^2}(\phi^2_{\text{av}}) \propto \int d\phi' e^{-H_{m_1^2}(\phi')} \delta(\phi'^2_{\text{av}} - \phi^2_{\text{av}}), \tag{4.17}$$

where ϕ^2_{av} is the order parameter of a system and we have initially evaluated the distribution at m_1^2.

We can now reweight this histogram at some other value m_2^2

$$P_{m_2^2}(\phi^2_{\text{av}}) \propto P_{m_1^2}(\phi^2_{\text{av}}) e^{-(m_2^2 - m_1^2)H}. \tag{4.18}$$

It might be easier to think of this via partition functions instead. Let us start by defining a partition function for a scalar field theory

$$Z_m = \int \mathcal{D}\phi \ \exp\left(- \underbrace{\int_x \frac{1}{2}\partial^2\phi + \frac{1}{2}m^2\phi^2 + \frac{1}{4!}\lambda\phi^4}_{H_0} \right) \tag{4.19}$$

Now if we think about the partition function for some other mass m'

$$Z_{m'} = \int \mathcal{D}\phi \ \exp\left(- \int_x \frac{1}{2}(m'^2 - m^2)\phi^2 - H_0(m) \right), \tag{4.20}$$

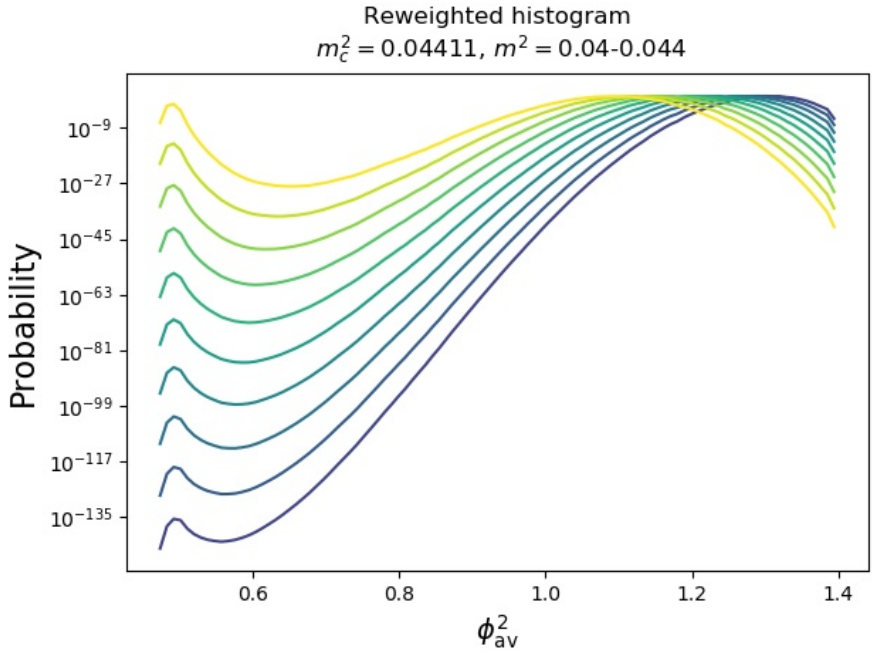

Figure 4.2: Reweighted histograms, original probability is calculated around $m^2 = 0.043$ with a 60^3 lattice. See how the relative height of the peaks changes, the lower the mass the more suppressed the symmetric peak is. The $m^2 = 0.044$ is visualised in yellow and $m^2 = 0.04$ corresponds to the lowest dark blue line.

we can clearly see that in our case the probability distribution can be reweighed as

$$P_{m_2^2}(\phi^2_{\mathrm{av}}) \propto \exp\left[-\frac{V}{2}(m_1^2 - m_2^2)\phi^2_{\mathrm{av}}\right] P_{m_1^2}(\phi^2_{\mathrm{av}}). \tag{4.21}$$

The proportionality constant can be found by normalising the probability distribution

$$\int d\phi^2_{\mathrm{av}}\ P(\phi^2_{\mathrm{av}}) = 1. \tag{4.22}$$

See Fig. 4.2 for an example on what a reweighted histogram looks. Using reweighting it is easy to determine the critical mass, where the peaks are equally high, and the probability of tunneling is equal. Since the histograms are relatively sensitive to a change of the mass parameter, reweigthing cuts down a lot of the computational costs.

4.2.5 Multicanonical Monte Carlo

Normally, Monte Carlo simulations use the Boltzmann weight $\propto \exp(-\beta H)$ to sample the configuration in thermal equilibrium. However, there are certain cases when this is not the best method of approach. One of these cases are first order PTs, where we want to determine the amount of tunneling. Thus, we want to sample between the different phases, the problem being that in the middle the probability is exponentially suppressed. To guarantee that we also tunnel between the phases we need to use multicanonical Monte Carlo simulations where instead of the Boltzmann weight we introduce an additional weight function $W(M)$. It is technically possible to sample the configuration also just with the Boltzmann weight, however that would be very costly. The multicanonical method speeds things up while still ending up back in the Boltzmann distribution.

The general idea behind this is relatively straightforward: flatten the probability distribution so you can sample it all. Then you plug back the weight function to get the real probability distribution, see Figs. 4.3 and 4.4.

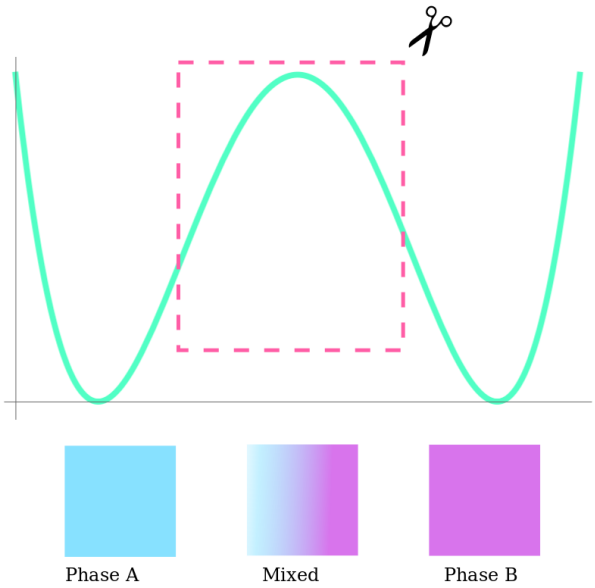

Figure 4.3: The multicanonical MC can be though as of cutting off the middle peak so that it is easier to sample the mixed phase configurations. After the sampling is done we can glue the peak back in. This is analogous to reweighting section, we use the weight function to get the proper distribution.

- Use the modified probability $p \propto \exp(-\beta E + W(M))$ to sample your configuration. $W(M)$ is the weight function.
- The probability produced by the simulation is then $p_{\text{muca}}(M) \propto p_{\text{can}}(M)e^{W(M)}$
- To get the canonical distribution we perform reweighting $p_{\text{can}} \propto p_{\text{muca}}(M)e^{-W(M)}$.
- A common parametrisation of $W(M)$ is a linear piecewise one. We divide the parameter into bins so that for bin i, $w_i = W(m_i)$

$$W(M) = w_{i+1}\frac{M - m_i}{m_{i+1} - m_i} + w_i\frac{m_{i+1} - M}{m_{i+1} - m_i} \quad M \in [m_i, m_{i+1}]. \tag{4.23}$$

4.3 Non-equilibrium lattice techniques

4.3.1 Real time evolution

For the real time evolution we chose to use the leapfrog algorithm, mainly because it is second order accurate and is reasonably quick to implement [59]. We will now also define π as the momentum field in the system. The algorithm gets its name from the children's game, since ϕ jumps over π when going forwards in time, see Fig. 4.5.

We start by introducing the reader to the simplest form of leapfrog and then add noise and damping terms later on. We evolve the fields according to the Hamiltonian stochastic equations

$$\partial_t \phi_a(x,t) = \pi_a(x,t) \tag{4.24}$$

$$\partial_t \pi_a(x,t) = -\frac{\delta H_0}{\delta \phi_a}, \tag{4.25}$$

where we will define the exact form of $\frac{\delta H_0}{\delta \phi_a}$ later since it depends on the theory. Written on lattice these equations become

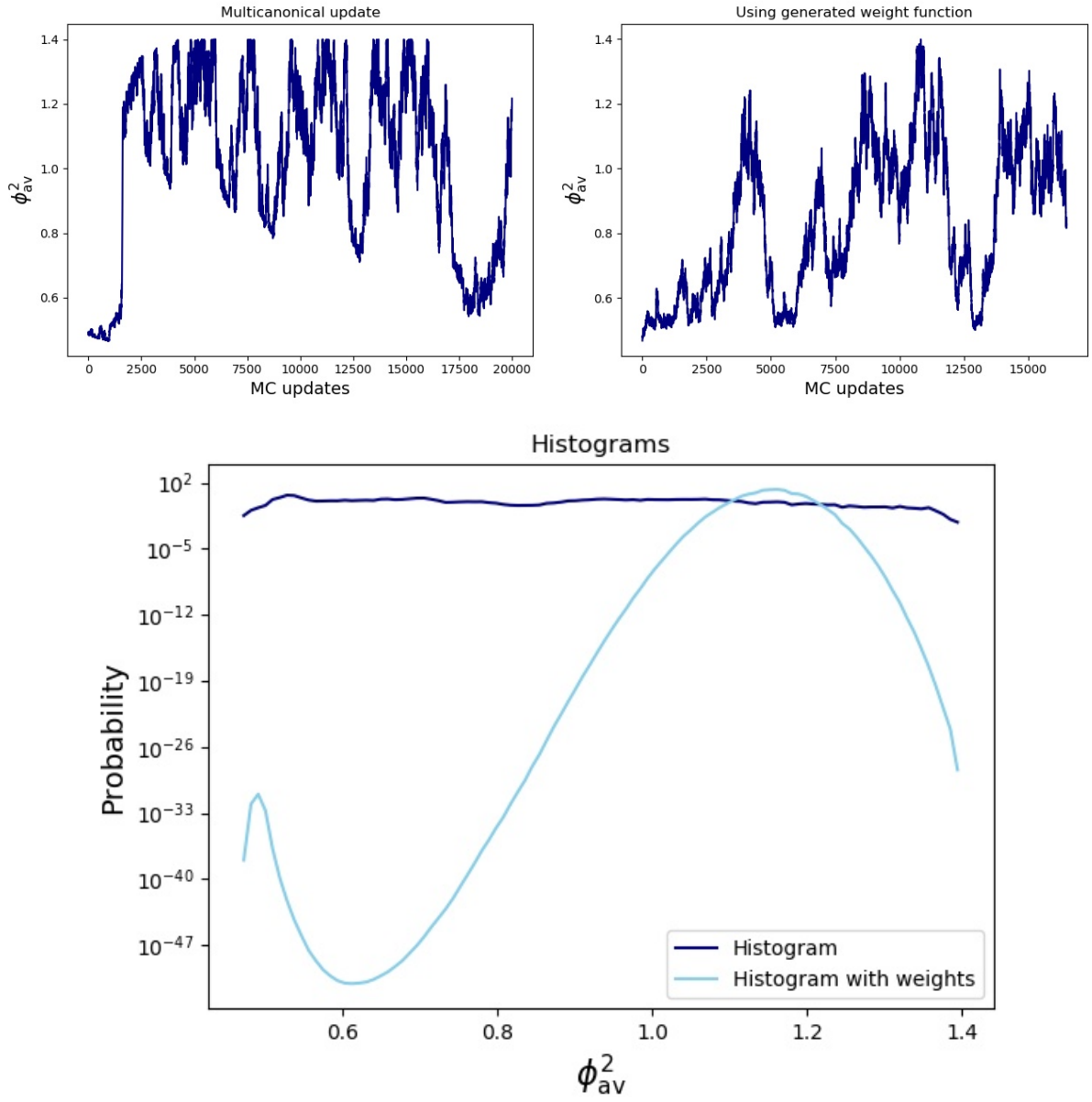

Figure 4.4: Example of a multicanonical MC run with a 60^3 lattice. At the top we show the Monte Carlo update history of the runs, where the weight function is generated (right) and where we are using the weight function we just generated (left). Ideally we want to sample the whole range of order parameters ϕ^2_{av} as well as possible. The histograms (bottom) show how much of a difference the weight function makes. We can clearly see the two peaks of the phases as well as the critical point when using the weighted histogram.

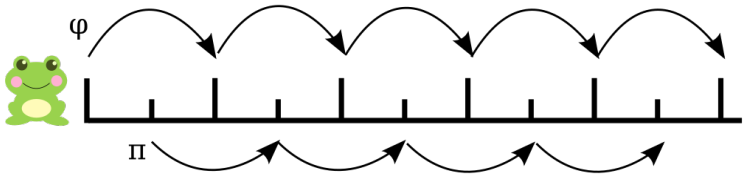

Figure 4.5: The leapfrog algorithm, the ϕ field hops over the momentum field π. One has to be careful when measuring observables that depend on both ϕ and π.

$$\phi_t(x,t+1) = \phi_a(x,t) + \pi_a(x,t) \tag{4.26}$$
$$\pi_a(x,t+1) = -\frac{\delta H_0}{\delta \phi_a} + \pi_a(x,t). \tag{4.27}$$

The standard leapfrog is therefore

$$\phi_{a,n+1} = \phi_{a,n-1} + \pi_{a,n+1/2}\Delta t \tag{4.28}$$
$$\pi_{a,n+1/2} = -\frac{\delta H_0}{\delta \phi_a}\Delta t + \pi_{a,n-1/2}. \tag{4.29}$$

The slightly more complicated case is the one where we have to consider the effects of the noise and damping in the real time evolution. We use the Crank-Nicholson method [60] to take the damping term into account. The Hamiltonian stochastic equations now read

$$\partial_t \phi_a(x,t) = \pi_a(x,t) \tag{4.30}$$
$$\partial_t \pi_a(x,t) = -\frac{\delta H_0}{\delta \phi_a} + \gamma \pi_a(x,t) + \xi_a(x,t), \tag{4.31}$$

where we have added the Gaussian noise term ξ_a and the damping term γ.

Since the noise is Gaussian it satisfies the condition

$$\langle \xi_a(x,t)\xi_b(x',t')\rangle = 2\gamma\delta_{ab}\delta(t-t')\delta^3(x-x'). \tag{4.32}$$

Written to the lattice these equations become

$$\phi_t(x,t+1) = \phi_a(x,t) + \pi_a(x,t) \tag{4.33}$$
$$\pi_a(x,t+1) = -\frac{\delta H_0}{\delta \phi_a} + (\gamma+1)\pi_a(x,t) + \xi_a(x,t). \tag{4.34}$$

In our case, writing the equations of motion for the system using the leapfrog integration read

$$\phi_{a,n+1} = \phi_{a,n-1} + \pi_{a,n+1/2}\Delta t \tag{4.35}$$
$$\pi_{a,n+1/2} = -\frac{\delta H_0}{\delta \phi_a}\frac{\Delta t}{1+\gamma\frac{\Delta t}{2}} + \frac{1-\gamma\frac{\Delta t}{2}}{1+\gamma\frac{\Delta t}{2}}\pi_{a,n-1/2} + \frac{\Delta t}{1+\gamma\frac{\Delta t}{2}}\xi_a. \tag{4.36}$$

To satisfy the condition in E.q (4.32) we draw values from a Gaussian distribution with standard deviation

$$\sigma = \sqrt{\frac{2\gamma}{a^3\Delta t}}. \tag{4.37}$$

One should put extra care into initialising the momentum field correctly, since it can affect the thermodynamics dramatically. When measuring energy (or anything that depends both on ϕ and π fields) one should also pay attention to making sure that the fields are at the same time step, since the energy depends on both fields, see Eq. (6.6). This means implementing a so called kick-drift-kick format of leapfrog. In the kick-drift-kick formalism the momentum update is switched to

$$\pi_{a,n+1/2} = -\frac{\delta H_0}{\delta \phi_a}\frac{\Delta t}{\frac{1}{2}+\gamma\frac{\Delta t}{8}} + \frac{1-\gamma\frac{\Delta t}{4}}{1+\gamma\frac{\Delta t}{4}}\pi_{a,n-1/2} + \frac{\Delta t}{\frac{1}{2}+\gamma\frac{\Delta t}{8}}\xi_a \tag{4.38}$$

So in contrast to the normal leapfrog, we first evolve the momentum field half a step, then normally ϕ and then do half a momentum field update again.

In Fig. 4.7 we can clearly see that the smaller the time step, the less fluctuations we have in the leapfrog method, as we should. The energy should be conserved when $\gamma = 0$. In

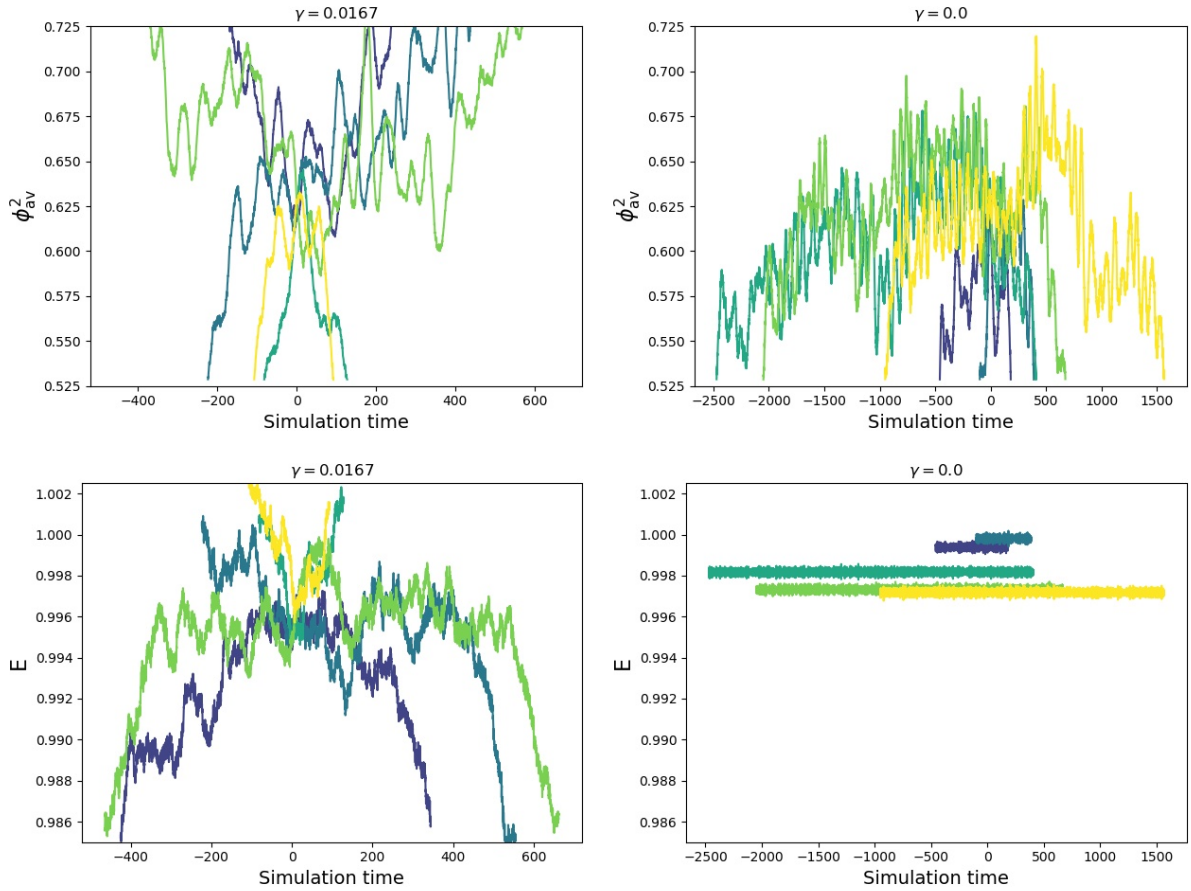

Figure 4.6: Trajectories of the order parameter and the energy for a 60^3 lattice. Note that the initial momenta are the same but the field configurations are different, hence the differences in energy. With the damping $\gamma = 0$ the energy is conserved and the trajectories fluctuate a long time around the critical value. The y-axis (top) is the value of the order parameter.

the simulation code we first initialise the momentum half update and the proceed with normal leapfrog, this due to the fact that normal leapfrog is considerably faster than kick-drift-kick.

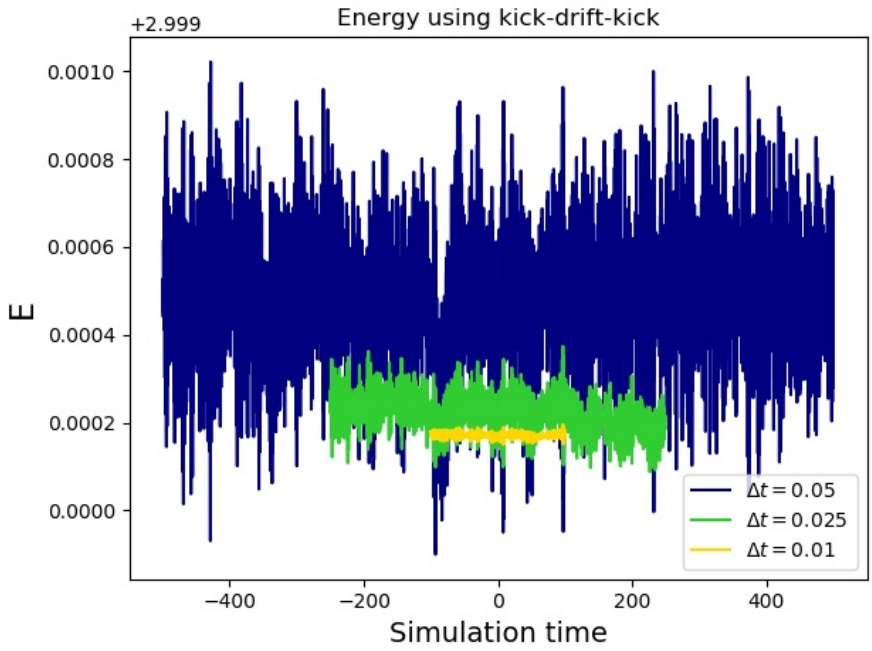

Figure 4.7: The energy of the system using kick-drift-kick algorithm with a 22^3 lattice. Note that the energy is conserved without the damping term. We see a clear difference when we measure the energy at smaller Δt.

4.4 Measurements and error analysis

4.4.1 Measured parameters

The important parameters measured from the Monte Carlo part of the code are the order parameter θ and the separatrix field values. The definition of order parameter is theory-dependent but for the cubic anisotropy model we have used the average of the two fields

$$\theta = \phi^2_{\text{av}} = \phi^2_1 + \phi^2_2. \tag{4.39}$$

The separatrix fields are field configurations where the order parameter is near the critical bubble, these configurations will be used later in the real time evolution part of the code, see Chapter 5 for more information.

We will now briefly discuss how to determine whether the mix of different MC algorithms

we use is reliable and independent enough to be used in the simulation. Additionally, we also discuss the importance of error analysis when measuring observables, such as the order parameter.

4.4.2 Autocorrelation

Autocorrelation describes how strongly successive steps depend on each other. It roughly tells us how many MC updates we need in order to get measurements to be independent of each other. To eliminate these dependencies the autocorrelation function should fluctuate around zero. The function is defined as

$$c_k(x) = \frac{\sum_{i=1}^{N-k}(x_i - \bar{x})(x_{i+k} - \bar{x})}{\sum_{i=1}^{N}(x_i - \bar{x})^2}, \tag{4.40}$$

where $\bar{x}$ is the average of some observable x.

In the simulations we have used an algorithm that is a mix of metropolis and overrelaxation, due to the autocorrelation dropping quickly to zero in the beginning, see Fig. 4.8.

4.4.3 Bootstrap and jackknife resampling methods

How do we estimate the errors of different quantities when there is no guarantee of them being independent? The standard way of doing error analysis would produce incorrect results if there exists bias in the data sets e.g. in the from of autocorrelation. The way to avoid this pitfall is to use resampling methods, where we generate new data sets from the original full data set. We use jackknife and bootstrap methods to estimate the errors. Both methods are considered to be the standard way of calculating the error from MC simulations for observable some x, but have minor differences on how they work. See Ref. [61] for a reference. We will now briefly describe both resampling methods.

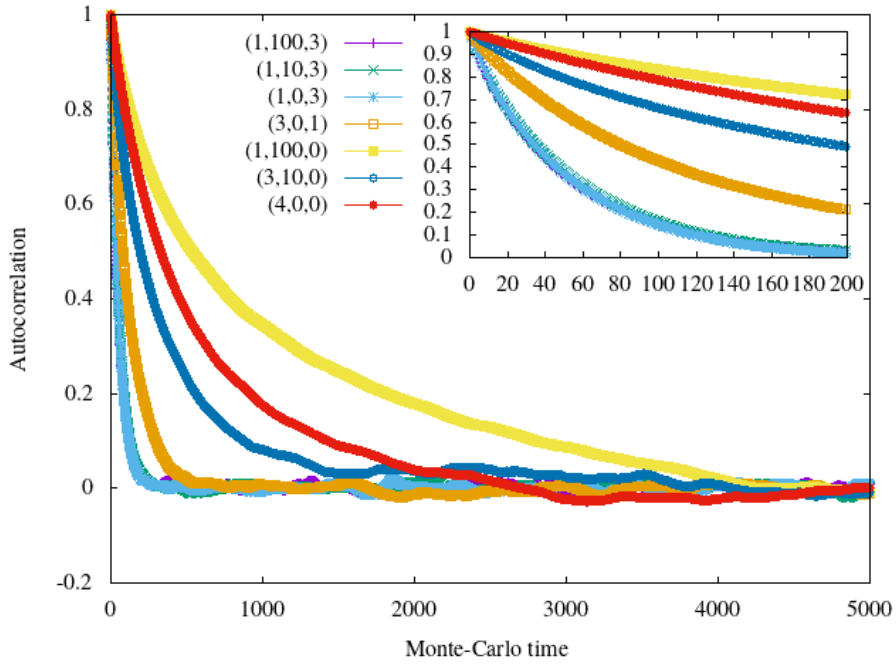

Figure 4.8: The autocorrelation using a different mix of algorithms and steps. The legend shows the number of steps each algorithm has (metropolis, radial metropolis, overralaxtion). So that (1,100,3) corresponds to 1 iteration Metropolis, 100 radial Metropolis and 3 overrelaxation steps. Credit: Oliver Gould.

Jackknife

The idea behind jackknife resampling is to divide the data into M blocks. Then for each $m = 1...M$ remove block m from the data and calculate the average of the observable $\bar{A}_m$ using the remaining data, see Fig 4.9. To get the standard deviation we use the generated resamples $\bar{A}_m$

$$\delta A = \sqrt{\frac{M-1}{M}\sum_{m=1}^{M}(\bar{A}_m - \bar{A})^2}, \tag{4.41}$$

where $\bar{A}$ is the average of the full data set.

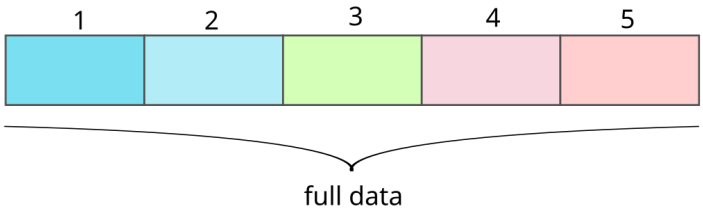

Figure 4.9: The full data divided into $M = 5$ blocks. Example data sets from full data set blocks created with jackknife: (2,3,4,5) and bootstrap: (1,1,4,5,3).

Bootstrap

Bootstrap is slightly more complicated but the idea remains the same. We divide the data to a set of M blocks. Now, instead of just taking away one block at the time we randomly pick the blocks to construct the new data, see Fig 4.9. We can also pick the block of data multiple times or not at all. Next we calculate the desired quantity B, for example an average. We repeat this N_B times so that we get a set of values B_i.

Occasionally the next step is to cut off the edges of this distribution of values B_i so that we are left with 68% of the values. Hence we want to determine the values a and b such that

$$\frac{\#B_i < a}{N_B} = 0.16 \quad \text{and} \quad \frac{\#B_i > b}{N_B} = 0.16 \tag{4.42}$$

and we can get the error as $\Delta B = (b - a)/2$.

However, usually cutting off the edges is not necessary and we can simply use

$$\delta B = \sqrt{\frac{1}{N_B - 1} \sum_i (B_i - \langle B \rangle)^2}, \tag{4.43}$$

where $\langle B \rangle = \sum_i \bar{B}_i / N_B$.

Chapter 5

Nonperturbative calculation of the bubble nucleation rate

The chapter is devoted to describing the bubble nucleation rate simulation as accurately as possible. We introduce all the necessary steps in order to calculate the full rate. This is done utilising the MC methods and the real time evolution introduced in the previous chapter.

The nucleation rate that can be determined by lattice calculations is [38]

$$\Gamma V \simeq P_C^{\epsilon} \frac{1}{2} \left| \frac{\Delta\theta}{\Delta t} \right| \langle \mathbf{d} \rangle, \tag{5.1}$$

where P_C is the probability distribution acquired from the multicanonical MC simulations, and $\left|\frac{\Delta\theta}{\Delta t}\right|$ and $\langle \mathbf{d} \rangle$ are the dynamical factors.

The evaluation of the nucleation rate is done in two parts:

1. Determining the probability distribution.

2. Calculation of the dynamical factor using real time evolution.

In Fig. 5.1 we have illustrated how the calculation proceeds. We will now go through the evaluation of both the probability distribution and the dynamical factors. The aim of this chapter is to tie the calculation, and the previously introduced different Monte Carlo methods and real time evolution, together.

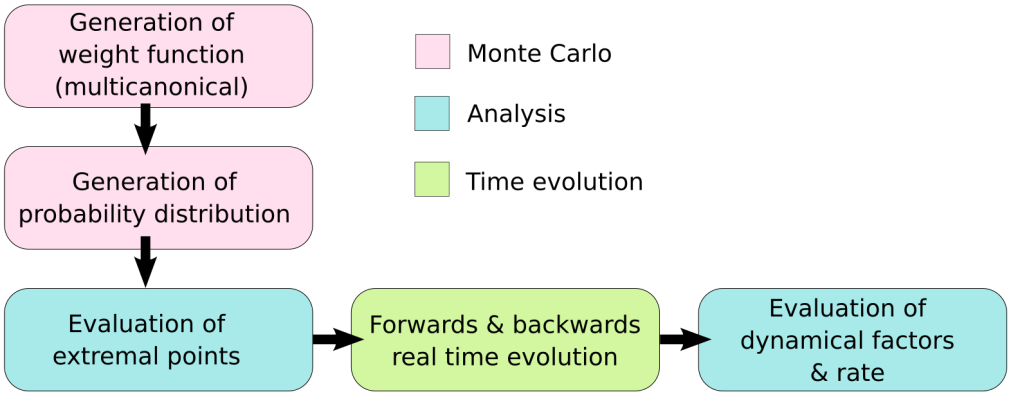

Figure 5.1: The calculation in a nutshell. The Monte Carlo phase consists of the equilibrium techniques shown in Section 4.2 and the time evolution uses the real time evolution introduced in Section 4.3. The analysis parts of the calculation pipeline are done separately from the main simulation code.

5.1 Probability

The probability distribution from which we draw the field configurations is produced in two parts. As mentioned earlier, the probability is highly peaked around the pure phases and without the multicanonical update discussed earlier in Section 4.2.5 we would never properly sample the mixed phase. We would start from either of the phases and be indefinitely stuck there for the rest of the simulation. To avoid that, we first run the MC code using the multicanonical update. This generates a weight function that we can use for reweighting the probability distribution correctly in the end, see Fig. 5.2.

We run the MC code again, this time not updating the weight function but instead using the one we just generated. We can now pick a narrow range ϵ around the peak of the weight function that corresponds to the critical bubble θ_C, namely $[\theta_C - \epsilon/2, \theta_C + \epsilon/2]$ and draw field configurations from this range. We call these the separatrix field configurations and they work as the initial field configurations we use in the real time evolution code. The critical bubble is defined to be an ensemble of field configurations where we are equally as likely to fall either to the symmetric or to the broken phase [37]. In general, the algorithm for both steps of the Monte Carlo code (namely updating the weight function and reading

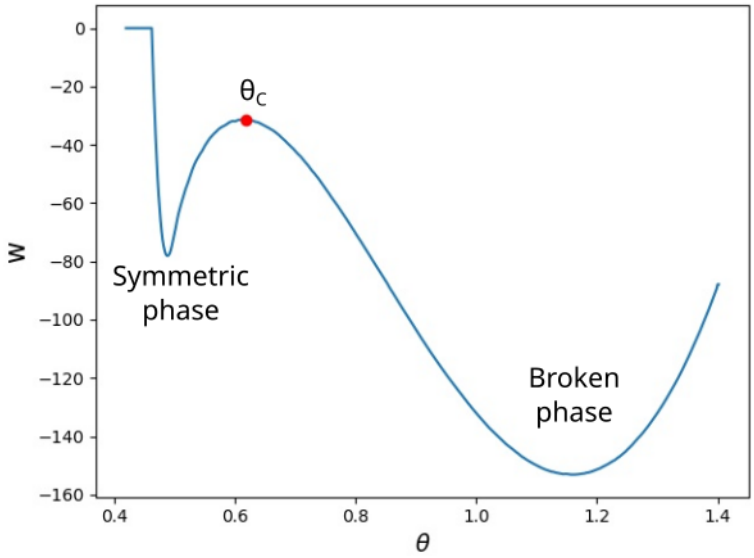

Figure 5.2: Example of a weight function (w) after the multicanonical update run plotted against the order parameter. It is used to determine the exact location for the critical bubble θ_C.

in the weight function) can be described by:

- Start by picking values for the coupling constants, namely m^2, λ_a.
- Generate field configurations using the mix of different MC update methods. Calculate the order parameter θ.
- Sample the configuration space until the chosen order parameter range is sampled well enough.
- Form a histogram of the measurements which can be normalised to get a probability distribution.

The next step is to use reweighting to determine the critical mass, where the peaks of symmetric and broken phase are equally probable, meaning they have the same height. Then we reweight the histogram to different mass parameters, see Section 4.2.4, this reduces the runs we need to do for different mass parameters, the mass ranges also tend to be quite narrow for tunneling, see Fig. 5.3. To get the probability contribution in Eq.

(5.1) we normalise the probability of the critical phase to the symmetric phase. Thus, we get

$$P_C^{\epsilon} = \frac{P_C}{\epsilon P_S}, \tag{5.2}$$

where

$$P_C = \int_{\theta-\epsilon/2}^{\theta+\epsilon/2} d\theta \; P(\theta) \quad \text{and} \quad P_S = \int_0^{\theta_C} d\theta \; P(\theta) \tag{5.3}$$

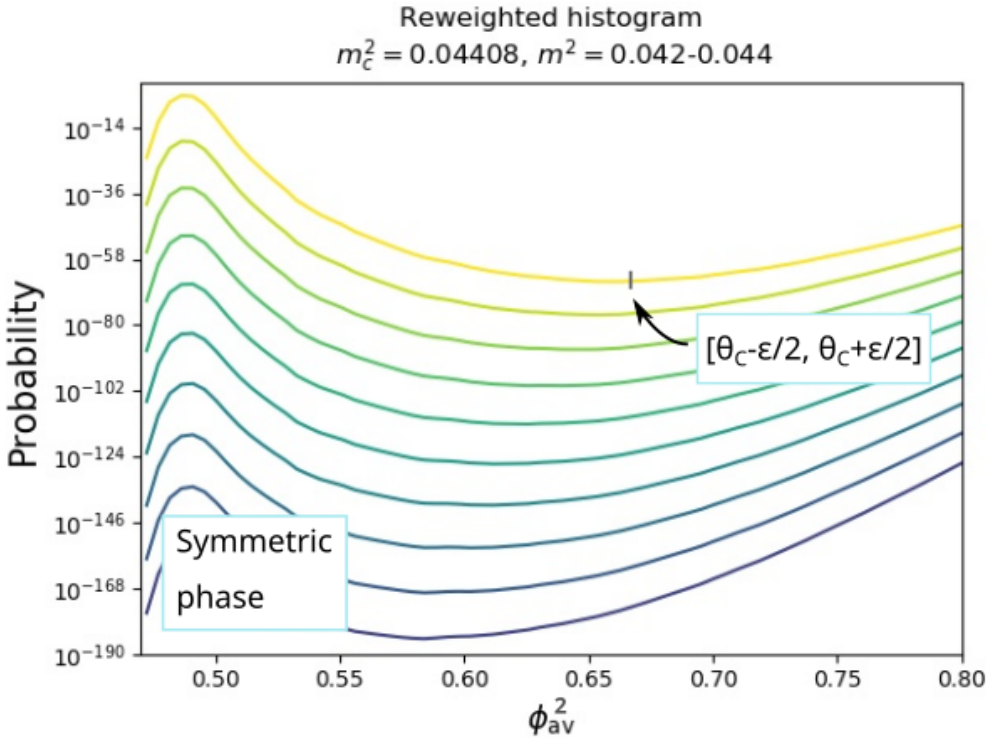

Figure 5.3: The reweighted probability distribution using a 80^3 lattice. We can see how the value of critical bubble varies with different mass parameters. We can now easily determine the ratio of the critical to symmetric phase. The value of ϵ is chosen so that it is a small range around the critical bubble.

5.2 Real time evolution parameters

5.2.1 The flux parameter

Here we specialise to our chosen order parameter $\theta = \phi^2_{\rm av}$. The flux parameter $\langle|\Delta\phi^2_{\rm av}/\Delta t|\rangle$ can be evaluated analytically and it is a short calculation which we give here. First, from the stochastic Hamiltonian equations we get that

$$\frac{\Delta\phi^2_{\rm av}}{\Delta t} = \frac{2}{V}\phi_a\pi_a. \tag{5.4}$$

The momentum π_a will behave like a Gaussian random variable at thermal equilibrium.

For Gaussian variables we have the following identities

$$\langle\pi_a(x)\pi_b(y)\rangle = \delta_{ab}\delta_{xy} \quad \text{and} \quad \langle f(\phi)g(\pi)\rangle = \langle f(\phi)\rangle\langle g(\pi)\rangle. \tag{5.5}$$

We need to evaluate $\langle|\Delta\phi^2_{\rm av}/\Delta t|\rangle$ at critical bubble $\phi^2_{\rm av,C}$, thus

$$\left\langle\left(\frac{\Delta\phi^2_{\rm av}}{\Delta t}\right)^2\right\rangle = \frac{4}{V^2}\langle\phi_a(x)\phi_b(y)\rangle\delta_{ab}\delta_{xy} = \frac{4\phi^2_{\rm av,C}}{V}. \tag{5.6}$$

We now can take the square root of the previous result and finally we get[1]

$$\left\langle\left|\frac{\Delta\phi^2_{\rm av}}{\Delta t}\right|\right\rangle = \sqrt{\frac{8\phi^2_{\rm av,C}}{\pi V}}. \tag{5.7}$$

We will now also include the factor 1/2 from Eq. (5.1) in this flux quantity so that we do not have to worry about missing factors of two later

[1]Note that we have used the known result for Gaussian numbers $\langle|x|\rangle = \sqrt{\frac{2}{\pi}\langle x^2\rangle}$.

$$\left\langle \left| \frac{\Delta\phi^2_{\rm av}}{\Delta t} \right| \right\rangle = \sqrt{\frac{2\phi^2_{\rm av,C}}{\pi V}}. \tag{5.8}$$

This part of the dynamical factor calculation is rather trivial, unfortunately we are still missing the non-trivial part.

5.2.2 The trajectories

Now we are only left with determining the remaining variable $\langle \mathbf{d} \rangle = \langle \delta_{\rm tunnel}/N_{\rm crossings} \rangle$. We need to evaluate the trajectories for the critical bubbles. When we start from the critical bubble we do not fall straight to either of the phases but order parameter fluctuates around the critical value. We need to determine two things, how many times we cross this critical value and whether or not we have tunneled. This part of the calculation uses the real time evolution algorithm introduced earlier. The calculation can done roughly as follows:

- Start by initialising a random momentum field, for this we draw random numbers from a Gaussian distribution with $\sigma = a^{-3/2}$.
- Evolve the fields from the critical bubble configuration (separatrix configuration) that we have determined earlier from the MC run.
- We evolve this configuration forwards in time until it reaches either of the determined cut-off values for the symmetric and broken phases, see Fig. 5.4.
- We go back to the configuration we started with (critical bubble) and reverse momentum $\pi \to -\pi$. This can be thought as of evolving the fields backwards in time.
- We can now form a full trajectory by combining the backwards and forwards evolution. The system tunnels if the backwards and forwards evolution end up in different phases ($\delta_{\rm tunnel} = 1$). If not they both end up in the same phase. We also determine how many times we cross the critical bubble value $N_{\rm crossings}$ since the configuration

oscillates around the critical bubble before falling to either of the phases, see Fig. 5.5.

When then evaluating the $\langle \mathbf{d} \rangle$ for the numerical results we must remember to reweight each configuration. Since the initial field configuration for the real time evolution are from a range $[\theta - \epsilon/2, \theta + \epsilon/2]$ the weight function is also different for each configuration and this can vary up to multiple factors. Hence the final value of $\langle \mathbf{d} \rangle$ becomes

$$\frac{1}{N} \sum_i \frac{\delta_{\text{tunnel},i}}{N_{\text{crossings}}} \rightarrow \frac{\sum_i \frac{\delta_{\text{tunnel},i}}{N_{\text{crossings}}} e^{-w_i}}{\sum_i e^{-w_i}}, \tag{5.9}$$

where w_i is the weight for the ith field configuration.

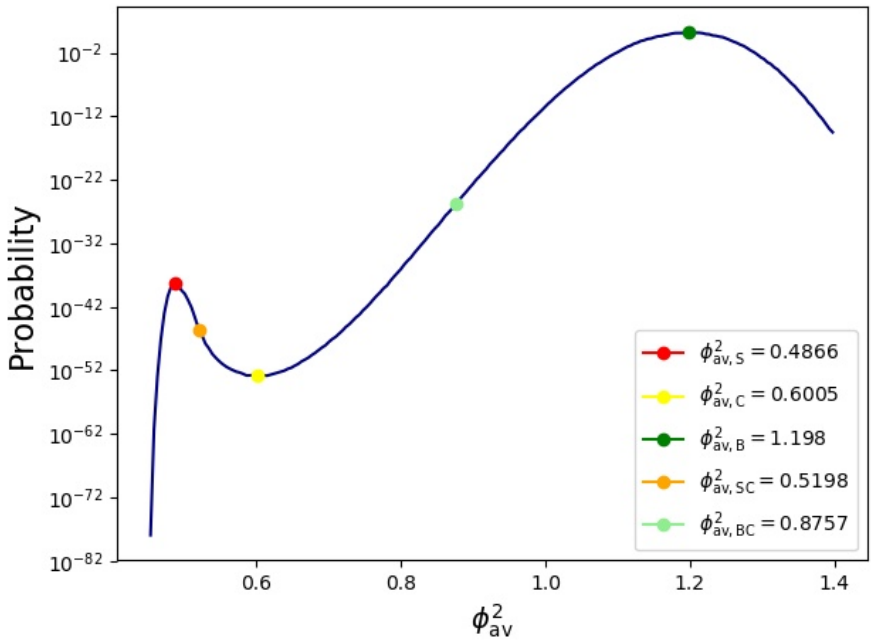

Figure 5.4: The probability distribution with the order parameter values for the symmetric, critical and broken phase, as well as the midpoint cut-off values SC and BC, where the system is physically guaranteed to get stuck on the respective phase, a 60^3 lattice.

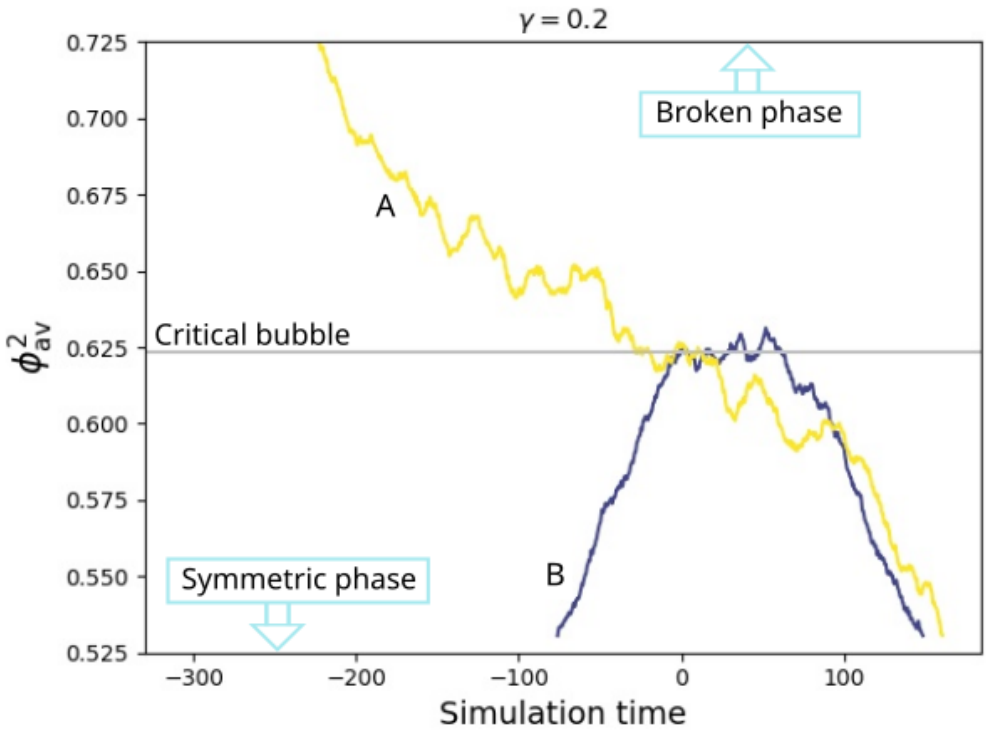

Figure 5.5: Real time evolution trajectory of a 80^3 lattice using leapfrog integration. The trajectory A tunnels and crosses the critical value 13 times. The trajectory B does not tunnel and crosses the critical value 16 times.

5.3 Noise

The noise term only affects the parameter $\langle \mathbf{d} \rangle$ since the probability and flux terms are independent of it. However, the noise term could significantly affect the value of $\langle \mathbf{d} \rangle$. To investigate the noise dependency we have plotted the dynamical factor $\langle \mathbf{d} \rangle$ against the noise magnitude

$$\epsilon = (1 - \exp(-2\gamma \Delta t)). \tag{5.10}$$

In Fig. 5.6 the behaviour of the noise is as expected, see Ref. [38]. We will use $\gamma = 1/L$ from now on in the results. When $\gamma = 0$ the system behaves as expected, the evolution is

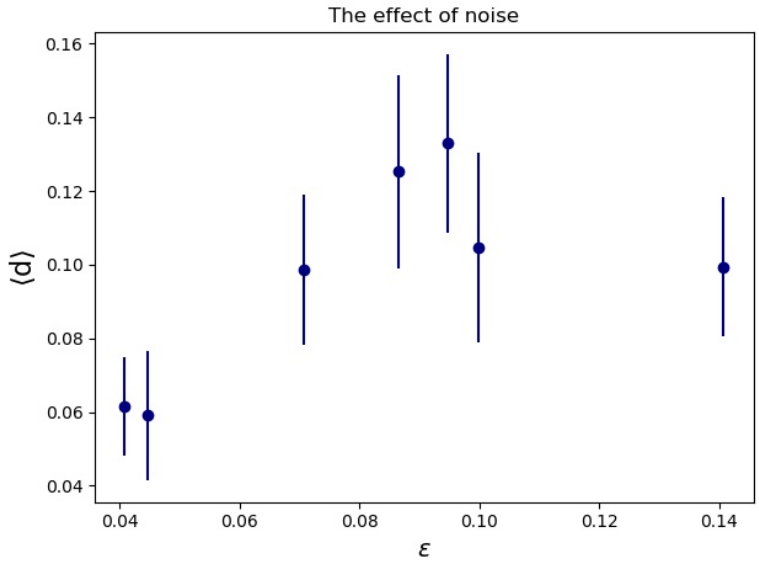

Figure 5.6: The noise magnitude, a 60^3 lattice, see Table 6.1 for the parameters used in different runs. The noise behaves similarly to results in Ref. [38] but is more prone to tunneling as one would expect with smaller volumes. Here we have used jackknife for the error bars.

purely Hamiltonian and the amount of tunneling is very small. The order parameter will mostly fluctuate around the critical bubble for a long time. One should also note that the bigger the lattice the smaller the effect of the overall noise will be, however the shape of the behaviour will stay the same regardless.

Chapter 6

Results from the nonperturbative calculation

After all these steps and different algorithms that go into the calculation, we have finally arrived at the results. We have simulated the cubic anisotropy model and calculated the nucleation rate. First we will briefly introduce the this model.

6.1 The cubic anisotropy model

To study the bubble nucleation rate nonperturbatively we wish to start with a simple toy model with a strong first order transition, namely the cubic anisotropy model. It is one of the simplest models to have a radiatively induced transition where the strength of the transition can be adjusted. This model has been studied before, see Ref. [38].

As usual the partition function determines the thermodynamics of the system

$$Z = \int \mathcal{D}\phi_2 \mathcal{D}\phi_2 \; e^{-H_0(\phi_1,\phi_2)}, \tag{6.1}$$

where the three-dimensional action is defined as

$$H_0(\phi_1, \phi_2) = \int d^3x \ \mathcal{L}(\phi_1, \phi_2). \tag{6.2}$$

The three-dimensional Euclidean Lagrangian of the system is given by

$$\mathcal{L}(\phi_1, \phi_2) = \frac{1}{2}[(\partial_i \phi_1)^2 + (\partial_i \phi_2)^2] + \frac{m^2}{2}[\phi_1^2 + \phi_2^2] + \frac{\lambda_1}{24}[\phi_1^4 + \phi_2^4] + \frac{\lambda_2}{4}\phi_1^2\phi_2^2, \tag{6.3}$$

where $\phi_{1,2}$ are the scalar fields, m is the mass term and $\lambda_{1,2}$ the couplings.

Written on the lattice the Lagrangian from Eq. (6.3) becomes

$$\begin{aligned}\mathcal{L} = \frac{Z_\phi}{2}(-\phi_1 \nabla_L^2 \phi_1 - \phi_2 \nabla_L^2 \phi_2) + \frac{Z_\phi Z_m (m^2 + \delta m^2)}{2}(\phi_1^2 + \phi_2^2) \\ + \frac{Z_\phi^2(\lambda_1 + \delta\lambda_1)}{24}(\phi_1^4 + \phi_2^4) + \frac{Z_\phi^2(\lambda_2 + \delta\lambda_2)}{4}\phi_1^2\phi_2^2,\end{aligned} \tag{6.4}$$

where Z_ϕ, Z_m, δm and $\delta\lambda_a$ are counterterms.

We can now give the exact form for the functional derivative $\delta H_0/\delta\phi_a$ that was previously seen in the stochastic Hamiltonian equations in Eq. (4.25). It is given by

$$\frac{\delta H_0}{\delta \phi_a} = -Z_\phi \nabla^2 \phi_a + Z_m(m^2 + \delta m^2)\phi_a + \frac{\lambda_1 + \delta\lambda_1}{6}\phi_a^3 + \frac{\lambda_2 + \delta\lambda_2}{2}\phi_a\phi_b^2, \tag{6.5}$$

where $a = 1, 2$.

The total Hamiltonian of the system is given by

$$H(\phi_a, \pi_a) = \int d^3x \ \frac{1}{2}(\pi_1^2 + \pi_2^2) + H_0(\phi_1, \phi_2), \tag{6.6}$$

and this is used when measuring the energy of the system, see the earlier discussion about the leapfrog and kick-drift-kick algorithm in Section 4.3.1. Note that the momentum fields only enter the simulation in the real time evolution part. This is the basis for the real

time evolution of the system.

Last but not least, the relationships between lattice and continuum quantities are

$$\phi_a = a^{-1/2}\phi_{a,L} \tag{6.7}$$
$$m^2 = a^{-2}m_L^2 \tag{6.8}$$
$$\lambda_a = a^{-1}\lambda_{a,L}. \tag{6.9}$$

6.2 The simulation parameters

Next, we will discuss the parameter choices we must make for the simulation. We start by defining λ_a. It determines what type of transition we will have, the possible choices are [38]:

- If $\lambda_1 > \lambda_2 > 0$ the transition would be of second order, which we obviously do not want.
- If $\lambda_2 = 0$ or $\lambda_2 = \lambda_1$ the transition is an Ising type transition.
- If $\lambda_2 < 0$ or $\lambda_2 > \lambda_1$ we finally have the desired first order PT. We choose $\lambda_2 = 8\lambda_1$, since this gives us a strong first order PT.

The value of $\lambda_{2,L}$ is tied to the lattice spacing, the smaller λ_L, the smaller the lattice spacing. So if we have initially set $\lambda_{2,L} = 2.5$ with 60^3 and we want to run a simulation with the same physical volume when $\lambda_{2,L} = 3$, we need a 50^3 box.

The second important parameter to choose is the value m_L^2, it should be chosen such that it is below the critical mass but not too far away, otherwise the symmetric phase will be suppressed. This can be done by picking some initial value for m_L^2 and then reweighting to see what is the reasonable choice. As we mentioned earlier the critical mass $m_{c,L}^2$ is the value when the peaks of symmetric and broken phase are of equal height. Table 6.1

V	$\lambda_{2,L}$	m_L^2	$m_{c,L}^2$
60^3	2.5	0.043	0.04411
80^3	2.5	0.043	0.04408
50^3	3	0.055	0.05724

Table 6.1: All the parameters used for the different MC runs, in lattice units. The value of $\lambda_{2,L}$ affects the choice of the lattice size and for a strong first order PT $\lambda_{1,L} = \lambda_{2,L}/8$. Note that here we do not give an error estimate for the critical mass.

contains all the used parameters for different runs.

In the real time evolution we always choose $\Delta t = 0.05$ and from now on the damping parameter is $\gamma = 1/L$, see Section 5.3 for discussion on the choice of varying γ.

6.3 The nucleation rate

Here we present the preliminary results for the nucleation rate, see Ref. [62] for the final results. In addition to plotting the nucleation rate we also want to investigate the behaviour of the free energy. The free energy of the system is defined as

$$F_c = -\ln P(\phi^2_{\mathrm{av,C}})/P(\phi^2_{\mathrm{av,S}}), \tag{6.10}$$

where unlike in Eq. (5.3) these are the probabilities at $\phi^2_{\mathrm{av,S}}$ and $\phi^2_{\mathrm{av,C}}$ respectively.

We have compared the nucleation rate and the free energy of the system at $\lambda_{2,L} = 2.5$ and $\lambda_{2,L} = 3$, see Fig. 6.1. However, it seems that the volumes we have used for these parameters have been too small and instead of a critical bubble configuration, we may have a critical cylinder. Fig 6.2 illustrates what will happen if the physical volume of the box is too small. This is illustrated especially well on Section 7.1 where we compare the simulation results to the thin-wall approximation.

It is noteworthy that a 60^3 lattice with $\lambda_{2,L} = 2.5$ and 50^3 with $\lambda_{2,L} = 3$ have the same

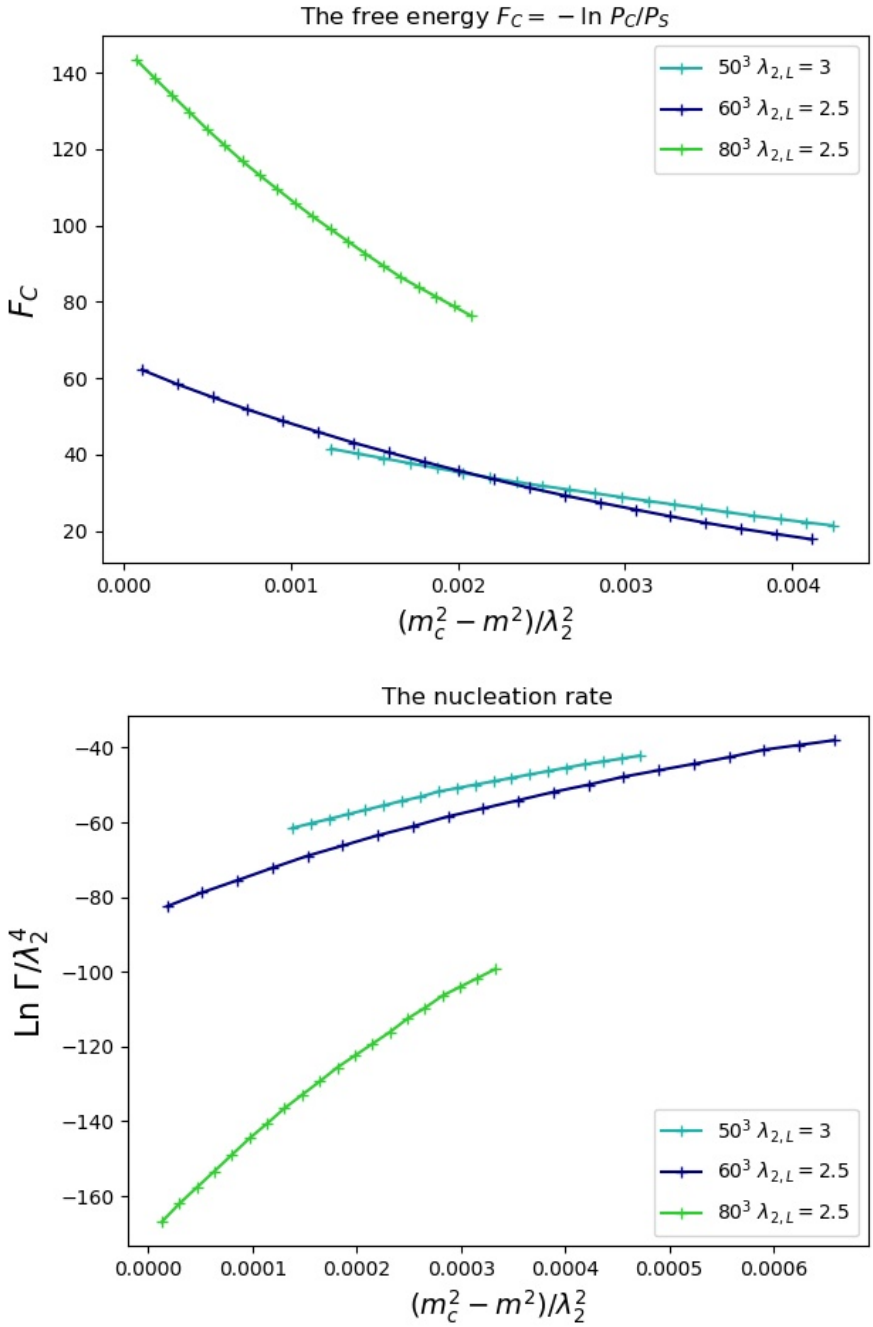

Figure 6.1: The free energy (top) and the nucleation rate (bottom). The nucleation rate is smaller at bigger volumes and the free energy bigger, as one would expect.

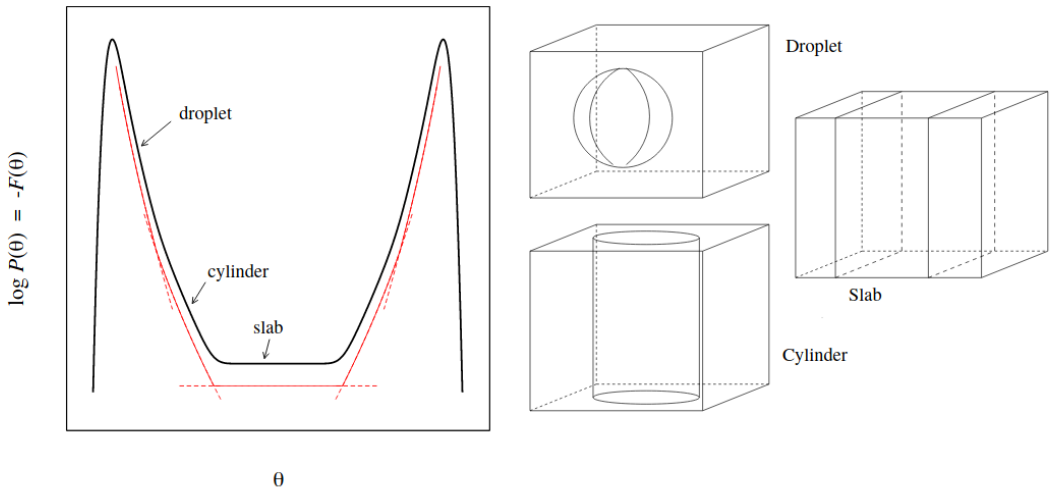

Figure 6.2: Depending on the box size, the critical bubble might not fit into the box, if this is the case, then instead of a bubble we will have a cylinder or a slab configuration. The thin wall approximation is visualised by the thin red lines. Image from Ref. [38].

physical volume, hence we can draw the conclusion that the lattice does not affect the results notably. However, when we keep the lattice spacing fixed by setting $\lambda_{2,L} = 2.5$ the difference between 60^3 and 80^3 is notable. This suggests that finite volume effects are rather large.

From a physical perspective, one would also expect that the larger volumes have a smaller tunneling rate. With smaller volumes the system is more likely to tunnel whereas with bigger volumes it takes longer to reach either of the phases. However, it is clear that in the future we will need to go to even bigger lattice sizes in order to guarantee a bubble configuration, instead of the current cylindrical one.

In Fig. 6.3 we can clearly see the difference the dynamical factors make in the calculation of the nucleation rate. Therefore, it is not enough to approximate the rate with only just the probability part as the full calculation does notably correct the value.

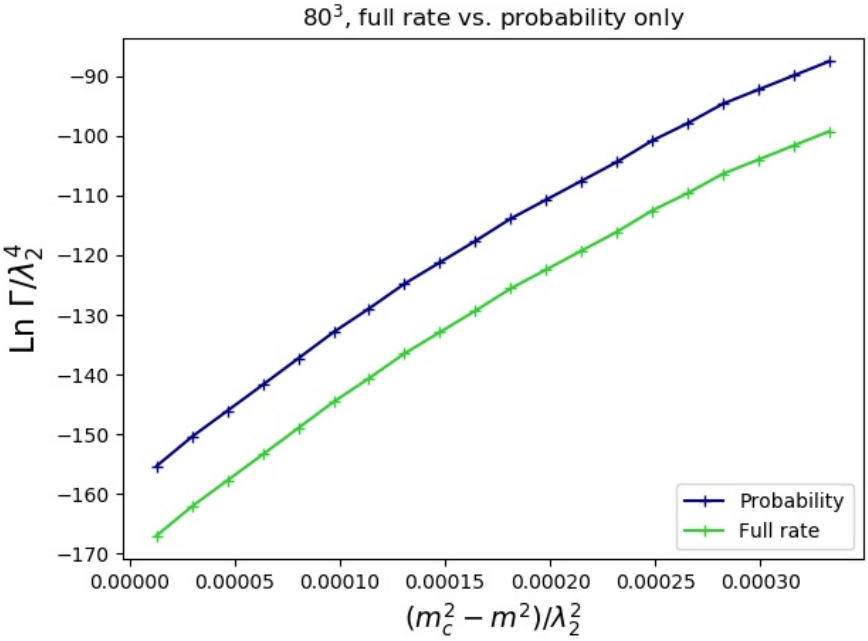

Figure 6.3: The difference the calculation of the dynamical factor of the nucleation rate makes. Probability part is calculated using the Monte Carlo part of the code using Eq. (5.2). The full rate contains the dynamical information.

Chapter 7

Discussion and conclusions

7.1 Comparison with perturbation theory

We compare our nucleation rate to the one that can be calculated using the thin-wall approximation and perturbation theory at leading-order (LO). The perturbative elements of the computation shown here closely follows Ref. [38], see there for further details on the perturbative approach. The calculation here follows that of the thin-wall approximation, except that we evaluate the surface tension σ and the energy difference between the symmetric and broken phase ϵ using perturbation theory.

First, we can allow the transition to happen in the direction of the ϕ_1 field and we shift $(\phi_1, \phi_2) \to (\phi_1 + x, \phi_2)$. Now looking at the potential from Eq. (6.3), the tree-level potential is

$$V_0(x) = \frac{1}{2}m^2x^2 + \frac{1}{4!}\lambda_1 x^4. \tag{7.1}$$

The 1-loop potential is

$$V_1(x) = -\frac{1}{12\pi}(m_1^3 + m_2^3), \tag{7.2}$$

where

$$m_1^2 = m^2 + \frac{1}{2}\lambda_1 x^2 \quad \text{and} \quad m_2^2 = m^2 + \frac{1}{2}\lambda_2 x^2. \tag{7.3}$$

Now to leading-order the potential is

$$V_{\mathrm{LO}}(x) = V_0(x) + V_1(x). \tag{7.4}$$

However, at leading-order we can simply ignore the m^2 term in the expression for m_2^2 and reduce the potential to

$$V_{\mathrm{LO}} = V_0(x) - \frac{1}{24\sqrt{2}\pi}\lambda_2^{3/2}x^3, \tag{7.5}$$

and from now on we will use this definition.

The surface tension is defined as

$$\sigma = \int_{x_{\mathrm{symmetric}}}^{x_{\mathrm{broken}}} dx\sqrt{2V_{\mathrm{LO}}(x)}. \tag{7.6}$$

We know that the symmetric phase is located at $x_{\mathrm{symmetric}} = 0$. We need to find σ, which can be done for first solving for the broken phase value of x, by finding the minima of the LO potential. Finding the critical mass m_c^2 can be done by setting

$$V_{\mathrm{LO}}(x_{\mathrm{broken}}) = 0. \tag{7.7}$$

The surface tension is evaluated only at T_c. It can be approximated by

$$\sigma \approx \frac{\lambda_2^{9/2}}{192\sqrt{6}\pi^3\lambda_1^{5/2}}. \tag{7.8}$$

At leading-order we found the following numerical values for the parameters

$$\begin{aligned} m_c^2 &= 0.0528 \\ x_{\text{broken}} &= 1.42 \\ \sigma/\lambda_2^2 &= 0.124. \end{aligned} \tag{7.9}$$

We can now calculate ϵ and find a relationship between the LO potential and δm^2 by expanding Eq. (7.5) as series

$$\epsilon \approx \frac{\delta m^2 \lambda_2^3}{16\pi^2 \lambda_1^2}. \tag{7.10}$$

Since we are working in the thin-wall approximation, we can use Eq. (2.47) to calculate the free energy. Thus we can approximate the nucleation rate as

$$\Gamma = m^4 e^{-S_3}. \tag{7.11}$$

Now we can easily compare the results from the simulations to the nucleation rate acquired from the thin-wall approximation using LO perturbation theory to evaluate σ and ϵ, see Fig. 7.1. One would expect for the perturbative approximation to fare worse than the simulations. This is generally the case, see Ref. [38], but as we can see the simulations suggest not as promising results as suggested by the earlier work. Qualitatively, the simulations and the thin-wall approximation have the same shape, but there is an offset to the simulation results. This may be due to the fact that the volumes we have used in the simulations are too small to fit the bubble and instead we end up with a cylindrical configurations.

However, to test the effects of the finite volume and of lattice spacing further investigation has to be done. This unfortunately will be beyond the scope of this thesis, purely out of the reason that the running simulations with larger lattices will take a considerable amount of time.

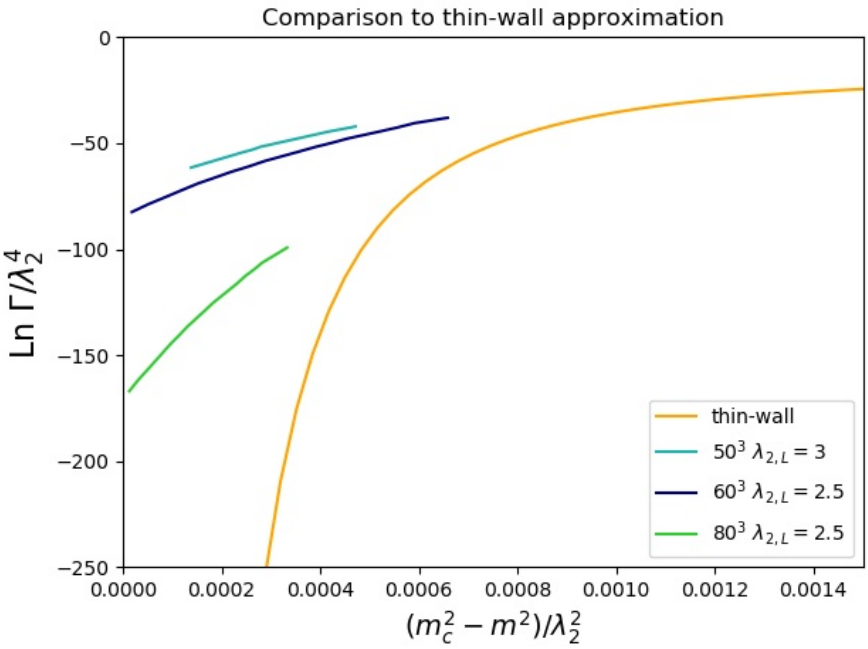

Figure 7.1: The comparison between the simulation results and the LO thin-wall approximation. There is an offset between the simulation and thin-wall results.

Also note that our results are not directly comparable with Ref. [38] since they have used the improved version of the action. It adds additional interaction terms to reduce lattice artefacts. We have used the unimproved version and these discrepancies may be explained by this. Furthermore, the LO correction to the potential is generally thought to give quite inaccurate results, the next-to-leading order (NLO) would possibly provide us with better results for comparison, as is suggested in Ref. [38].

7.2 Future work

In the future we hope to achieve a better understanding of the toy models we have studied. The results for the cubic anisotropy model are preliminary, and the for the singlet model the simulation code still requires some tweaking. We will instruct the reader to look for

Ref. [62] for the accurate results from these both models.

7.2.1 The real scalar theory

The other model we intend to investigate is the scalar singlet model that is a one component scalar field with a tree level-barrier. The main reasons why we have picked it are: it is a simple extension of the SM, the perturbative results are well known and we expect the lattice simulations to give more reliable answers on the nucleation rate than the perturbation theory. However, despite perturbative results being well known lattice calculations remain a rarity.

The Lagrangian of the singlet model is

$$\mathcal{L} = \frac{1}{2}(\partial_i \phi)^2 + \sigma\phi + \frac{1}{2}m^2\phi^2 + \frac{1}{3!}g\phi^3 + \frac{1}{4!}\lambda\phi^4 \tag{7.12}$$

and on the lattice it can be written as

$$\begin{aligned}\mathcal{L} = \frac{Z_\phi}{2}(-\phi\nabla_L^2\phi) + \frac{Z_\phi Z_m(m^2+\delta m^2)}{2}\phi^2 + (\sigma+\delta\sigma)Z_\phi^{1/2}\phi \\ + \frac{(g+\delta g)Z_\phi^{3/2}}{3!}\phi^3 + \frac{Z_\phi^2(\lambda+\delta\lambda)}{4!}\phi^4,\end{aligned} \tag{7.13}$$

where Z_ϕ, Z_m, δm^2, $\delta\sigma$ and δg are the counterterms.

The dimensionality of the parameters ϕ, m and λ remains the same as in the cubic model, with the addition of g and σ which become

$$\sigma = a^{-5/2}\sigma_L \tag{7.14}$$

$$g = a^{-3/2}g_L \tag{7.15}$$

The aim is to investigate the qualitative features it shares with currently popular extensions of the SM, where the additional field content has a tree-level barrier, like the Σ SM model [32]. Furthermore, the singlet model is easier to work with in perturbation theory

and gives opportunities to test its reliability, since it is a toy model where we can ignore gauge dependency problems. The singlet model will remain out of the scope of this thesis, but will be covered in future work, see Ref. [63].

7.3 Conclusions

The electroweak phase transition is a crossover in the Standard Model [13–15]. However, in many BSM theories it could be a first order transition. The EWPT remains as an attractive candidate since it could help to solve baryon asymmetry and possibly produce gravitational waves that could be detectable in the near future, one of these detectors is LISA [6] that is launching in the early 2030s. It would also provide us with more information about the electroweak epoch in general.

In this thesis we have briefly introduced the analytical calculation of the bubble nucleation rate and introduced the reader to a bounce solution at zero and finite temperatures. We have also gone through the thin-wall approximation, since it is a relatively easy way to acquire an approximation to compare our results to.

There are three different contributions to the possible GW signal from first order PT [44]: bubble collisions, sound waves and turbulence. The bubble collisions can be modelled with the envelope approximation but are only dominant in the true vacuum bubble case. Thus, sound waves and magnetohydrodynamic turbulence are more important and longer lasting sources of GWs. Sound waves are created by bubble moving in the primordial plasma and the MHD turbulence is due to percolation since the plasma is fully ionised. The sound waves are currently thought to be the dominating contribution, but this varies depending on the model. In this thesis we have investigated the cubic anisotropy model and while it can be used to study the nucleation rate, it cannot be used to produce a GW spectrum.

We have gone through the different tools and numerical methods we have used in order to calculate the nucleation rate and described the nonperturbative calculation in detail. The calculation is done in two parts. The Monte Carlo part of the code is used to eval-

uate the probability distribution for the used order parameter, and to create separatrix field configurations that can be used as initial conditions in the second part. The dynamical factors needed can be calculated using real time evolution, namely the leapfrog algorithm. We create trajectories that start from the separatrix configuration and evolve them in time until they reach either of the phases to determine whether the system has tunneled or not. The goal is to test the reliability of perturbation theory by comparing it to the simulation results. The results presented in this thesis are preliminary, and the reader is advised to look for future iterations of the work, see Refs. [62, 63].

The nucleation rate seems not to be affected much by the lattice effects, when keeping the physical size fixed but changing the lattice spacing the results are in good agreement. However, the finite volume effects are rather large, as seen when increasing the size from 60^3 to 80^3. It should also be noted, that unfortunately in our simulations we have used lattices that are too small. Therefore, we end up with cylindrical configurations instead of the desired bubbles and we are unable to fully demonstrate the capabilities of the simulations when compared to perturbation theory. Compared to the thin-wall approximation using parameters evaluated at-leading order, we would expect the simulations to perform better. All in all, to fully test the reliability of perturbation theory, more simulations with larger lattice sizes are needed.

Bibliography

[1] G. Aad, T. Abajyan, B. Abbott, *et al.*, Physics Letters B **716**, 1–29 (2012).

[2] S. Chatrchyan *et al.*, Physics Letters B **716**, 30–61 (2012).

[3] B. P. Abbott, R. Abbott, T. D. Abbott, *et al.*, Phys. Rev. Lett. **116**, 061102 (2016).

[4] R. Abbott, B. P.and Abbott, T. D. Abbott, *et al.* (LIGO Scientific Collaboration and Virgo Collaboration), Phys. Rev. Lett. **119**, 161101 (2017).

[5] B. P. Abbott *et al.*, The Astrophysical Journal **892**, L3 (2020).

[6] P. Amaro-Seoane *et al.*, "Laser interferometer space antenna," (2017), arXiv:1702.00786 [astro-ph.IM] .

[7] C. Caprini, M. Hindmarsh, S. Huber, *et al.*, Journal of Cosmology and Astroparticle Physics **2016**, 001–001 (2016).

[8] M. Kramer and B. Stappers, "Lofar, leap and beyond: Using next generation telescopes for pulsar astrophysics," (2010), arXiv:1009.1938 [astro-ph.IM] .

[9] S. Weinberg, Phys. Rev. D **9**, 3357 (1974).

[10] D. Kirzhnits and A. D. Linde, Annals Phys. **101**, 195 (1976).

[11] C. Caprini and D. G. Figueroa, Classical and Quantum Gravity **35**, 163001 (2018).

[12] M. Maggiore, *Gravitational waves : Volume 2, Astrophysics and cosmology* (Oxford University Press, 2018).

[13] K. Kajantie, M. Laine, K. Rummukainen, and M. Shaposhnikov, Physical Review Letters **77**, 2887–2890 (1996).

[14] M. Gürtler, E.-M. Ilgenfritz, and A. Schiller, Physical Review D **56**, 3888–3895 (1997).

[15] F. Csikor, Z. Fodor, and J. Heitger, Physical Review Letters **82**, 21–24 (1999).

[16] M. D'Onofrio and K. Rummukainen, Physical Review D **93** (2016), 10.1103/physrevd.93.025003.

[17] V. Kuzmin, V. Rubakov, and M. Shaposhnikov, Phys. Lett. B **155**, 36 (1985).

[18] C. Hogan, Mon. Not. Roy. Astron. Soc. **218**, 629 (1986).

[19] A. D. Linde, Phys. Lett. B **96**, 289 (1980).

[20] M. Shaposhnikov, Nuclear Physics B **287**, 757 (1987).

[21] M. Fukugita and T. Yanagida, Physics Letters B **174**, 45 (1986).

[22] W. Chao and M. J. Ramsey-Musolf, JHEP **10**, 180 (2014), arXiv:1406.0517 [hep-ph] .

[23] J. M. Cline, "Baryogenesis," (2006), arXiv:hep-ph/0609145 [hep-ph] .

[24] D. E. Morrissey and M. J. Ramsey-Musolf, New Journal of Physics **14**, 125003 (2012).

[25] P. A. Ade, N. Aghanim, M. Arnaud, M. Ashdown, J. Aumont, C. Baccigalupi, A. Banday, R. Barreiro, J. Bartlett, N. Bartolo, *et al.*, Astronomy & Astrophysics **594**, A13 (2016).

[26] A. Sakharov, Sov. Phys. Usp. **34**, 392 (1991).

[27] D. B. Kaplan, "Lecture notes in cosmology," (2004).

[28] M. S. Turner and E. W. Kolb, *The Early Universe* (Addison-Wesley, 1990).

[29] K. Kajantie, M. Laine, K. Rummukainen, and M. E. Shaposhnikov, Nucl. Phys. B **458**, 90 (1996), arXiv:hep-ph/9508379 .

[30] T. Gorda, A. Helset, L. Niemi, T. V. Tenkanen, and D. J. Weir, JHEP **02**, 081 (2019), arXiv:1802.05056 [hep-ph] .

[31] H. H. Patel and M. J. Ramsey-Musolf, JHEP **07**, 029 (2011), arXiv:1101.4665 [hep-ph] .

[32] L. Niemi, M. Ramsey-Musolf, T. V. Tenkanen, and D. J. Weir, (2020), arXiv:2005.11332 [hep-ph] .

[33] J. Langer, Annals of Physics **41**, 108 (1967).

[34] J. S. Langer, Annals of Physics **54**, 258 (1969).

[35] S. Coleman, Phys. Rev. D **15**, 2929 (1977).

[36] C. G. Callan and S. Coleman, Phys. Rev. D **16**, 1762 (1977).

[37] G. D. Moore and K. Rummukainen, Phys. Rev. D **63**, 045002 (2001), arXiv:hep-ph/0009132 .

[38] G. D. Moore, K. Rummukainen, and A. Tranberg, JHEP **04**, 017 (2001), arXiv:hep-lat/0103036 .

[39] S. Coleman, *Aspects of Symmetry: Selected Erice Lectures* (Cambridge University Press, 1985).

[40] M. Maggiore, *A Modern introduction to quantum field theory* (Oxford University Press, 2005).

[41] D. J. Gross, M. J. Perry, and L. G. Yaffe, Phys. Rev. D **25**, 330 (1982).

[42] A. D. Linde, Nucl. Phys. B **216**, 421 (1983), [Erratum: Nucl.Phys.B 223, 544 (1983)].

[43] M. Maggiore, *Gravitational waves : Volume 1, Theory and experiments* (Oxford University Press, 2008).

[44] D. J. Weir, Philosophical Transactions of the Royal Society A: Mathematical, Physical and Engineering Sciences **376**, 20170126 (2018).

[45] C. Caprini *et al.*, JCAP **03**, 024 (2020), arXiv:1910.13125 [astro-ph.CO] .

[46] A. Kosowsky and M. S. Turner, Physical Review D **47**, 4372–4391 (1993).

[47] D. Cutting, M. Hindmarsh, and D. J. Weir, Physical Review D **97** (2018), 10.1103/physrevd.97.123513.

[48] R. Jinno and M. Takimoto, Phys. Rev. D **95**, 024009 (2017), arXiv:1605.01403 [astro-ph.CO] .

[49] S. J. Huber and T. Konstandin, JCAP **09**, 022 (2008), arXiv:0806.1828 [hep-ph] .

[50] K. Farakos, K. Kajantie, K. Rummukainen, and M. Shaposhnikov, Nuclear Physics B **442**, 317–363 (1995).

[51] K. Kajantie, K. Rummukainen, and M. Shaposhnikov, Nuclear Physics B **407**, 356–372 (1993).

[52] K. Rummukainen, "Lecture notes in lattice simulation methods," (2003).

[53] K. Rummukainen, "Lecture notes in monte carlo simulation methods," (2008).

[54] M. Richey, American Mathematical Monthly **117**, 383 (2010).

[55] C. C. Hurd, Annals of the History of Computing **7**, 141 (1985).

[56] E. F. Schuster, The American Mathematical Monthly **81**, 26 (1974).

[57] K. Kajantie, M. Laine, K. Rummukainen, and M. E. Shaposhnikov, Nucl. Phys. B **466**, 189 (1996), arXiv:hep-lat/9510020 .

[58] A. M. Ferrenberg and R. H. Swendsen, Phys. Rev. Lett. **63**, 1658 (1989).

[59] B. Leimkuhler and S. Reich, *Simulating Hamiltonian Dynamics* (Cambridge University Press, 2004).

[60] J. Crank and P. Nicolson, Mathematical Proceedings of the Cambridge Philosophical Society **43**, 50–67 (1947).

[61] B. Efron, SIAM Review **21**, 460 (1979).

[62] O. Gould, A. Kormu, and D. J. Weir, In preparation.

[63] O. Gould, In preparation.